Dielectric effects, crystal field, and shape anisotropy tuning of the exciton fine structure of halide perovskite nanocrystals

A. Ghribi, S. Ben Radhia, K. Boujdaria, L. Legrand, T. Barisien, M. Chamarro, C. Testelin

Dielectric effects, crystal field, and shape anisotropy tuning of the exciton fine structure of halide perovskite nanocrystals

A. Ghribi,[1] S. Ben Radhia,[1] K. Boujdaria,[1,*] L. Legrand,[2] T. Barisien,[2] M. Chamarro,[2] and C. Testelin[2]

[1]*Université de Carthage, Faculté des Sciences de Bizerte, LR01ES15 Laboratoire de Physique des Matériaux : Structure et Propriétés, 7021 Zarzouna, Bizerte, Tunisia*

[2]*Sorbonne Université, CNRS, Institut des NanoSciences de Paris, F-75005, Paris, France*

(Received 2 June 2022; accepted 21 September 2022; published 3 October 2022)

We present a theoretical study of the excitonic band edge states applied to the more commonly studied inorganic perovskite nanocrystals: $CsPbBr_3$. We highlight the key role played by the electron-hole exchange interaction, including long-range and short range terms, in the positioning and splitting of dark and bright exciton sublevels, and discuss the influence of dielectric confinement, crystal field and shape anisotropy effects on the excitonic fine structure. The electron-hole exchange interaction splits the four excitonic states into three bright excitonic states at higher energy and a singlet dark state at lower energy. We find that, whatever the crystal phase, the bright-dark splitting is weakly sensitive to shape anisotropy. However, a strong enhancement, of about 50%, is obtained at the maximum of the dielectric contrast. For two crystalline symmetries, we particularly analyze how the bright exciton triplet energies vary, taking into account the states polarizations and considering the directions along which shape elongation/contraction applies. The main effect of the dielectric contrast is to increase significantly the exciton energies, for all the configurations. For a cubic crystal—O_h symmetry—the bright exciton triplet degeneracy can be partially or fully lifted with anisotropic shape along one or two directions, respectively. For a tetragonal crystal—D_{4h} symmetry—the partial triplet degeneracy can be completely lifted by a single distortion from the cubic shape along a direction perpendicular to the tetragonal axis but a partial degeneracy is maintained for small distortions along the tetragonal axis. The amplitude of bright exciton splittings are basically driven by the shape anisotropy and is almost insensitive to the dielectric contrast. On the basis of this model, we discuss recent results on $CsPbBr_3$ nanocrystals photoluminescence.

DOI: 10.1103/PhysRevMaterials.6.106001

I. INTRODUCTION

First promising results on the efficiencies of halide perovskite materials for photovoltaic cells were obtained at the beginning of 2010 [1–3], shortly followed by interesting results in a large variety of optoelectronic technologies such as light-emitting diodes [4–6], lasers [5,7,8] and photodetectors [9,10], and more advanced applications in spintronic domain [11–13] have attracted a huge interest in these materials. Moreover, the rapid progress in chemical synthesis has allowed the growth of strongly emitting metal halide perovskite nanocrystals (NCs) [14–18] with precise size, shape and composition control enlarging the domain of applications to quantum optics and quantum information.

In parallel to this extensive interest in applications, fundamental studies have also been developed in order to understand the electronic band structure and exciton main characteristics of bulk materials [19–24]. Metal-halide perovskite materials are direct band-gap semiconductors. In contrast to many other conventional semiconductors such as GaAs or CdSe, they show a reversed band ordering in the band gap diagram where the valence band maximum (VBM) and the conduction band minimum (CBM) are both described by anti-bonding combinations of the metal and halide orbitals: Pb s and Br p orbitals for the VBM with a total band state momentum $j_h = 1/2$; Pb p and Br s orbitals for the CBM [21,25]. Strong spin-orbit coupling affects mostly the conduction band and splits the electron states into an upper band with a total angular momentum $j_e = 3/2$ and a lower one with $j_e = 1/2$ (lowest split-off conduction band). The lowest optical transitions involve exciton states, electron-hole (e-h) pairs ($j_e = 1/2$ and $j_h = 1/2$) bound by the Coulomb interaction [26,27]. Due to its fundamental impact on efficient light emission and quantum technology, the physics of the excitonic fine structure (EFS) has been intensively investigated in the perovskite materials specially in nanostructures.

In bulk materials because perovskite materials can adopt different crystal phases [28–34], two main cases are distinguished regarding the structuration of the band edge exciton. For cubic crystal structure (with O_h as point group) the e-h exchange interaction (EI) splits the four degenerate exciton states in two groups of states: the optically active triplet state at higher energy with $j_{\text{exc}} = 1$ and a nonoptically active singlet state at lower energy. For tetragonal (D_{4h} point group) or orthorhombic (D_{2h} point group) phases, the bright exciton states are split as a consequence of the interplay between the anisotropic crystal field and the e-h EI and this splitting has been observed in bulk crystals [35].

*kais.boujdaria@fsb.rnu.tn

In 2015, the synthesis of inorganic lead halide, nearly cuboid-shaped NCs [36] was the culminating point of a research line on Pb doped cesium halide crystals initiated in the 1970s, opening the route to the synthesis of different perovskite nanomaterials [16]. The use of highly-resolved spectroscopic techniques, as the low temperature photoluminescence of a single NC, have revealed the bright states spectral signatures in different materials: $FAPbI_3$ [37], $FAPbBr_3$ [38,39], $MAPbI_3$ [40], $MAPbBr_3$ [41], $CsPbI_3$ [42,43], and the more studied $CsPbBr_3$ NCs [44–47] or NCs with alloy composition like $CsPb(Br_{1-x}Cl_x)_3$ [48,49]. In NCs the e-h EI is primarily enhanced by quantum confinement [24,50–53] hence the bright-states splittings are also enhanced with respect to the bulk situation. Because early photoluminescence experiments in single NCs revealed high efficiencies as well as a nonlinear behavior of the emission lines energies as a function of the applied magnetic field [44], it was suggested that a Rashba effect related to a local inversion symmetry breaking could be at play. In this picture the dynamical fluctuations of the Cs^+ ion positions in the inorganic perovskite lattice are responsible for a reversed splitting of the EFS sublevels placing the dark exciton state at higher energy [49]. However, early studies on $CsPbCl_3$ revealed that the Mn doping of these NCs enhances the bright state - dark state relaxation and led to photoluminescence dynamics consistent with a long-lived dark state placed at the lowest energy at cryogenic temperatures [54]. Moreover, in $FAPbBr_3$ [39] and $CsPbI_3$ [43], the lowest exciton state was shown to be optically activated thanks to magnetic coupling to the bright ones, which allowed to unambiguously demonstrate its "dark nature." Until now there are thus no direct experimental proofs in NCs of the reverse ordering proposed in Ref. [49]. In a latter publication, the authors of this claim have stated that the e-h EI enhancement in confined materials could overcome the perturbation caused by Rashba-like effects thought to predominate only in "larger size" NCs [55].

Over the last years NCs structures were explored and strongly non isotropic systems have also been engineered such as nanoplatelets or nanowires. Realizations show large variations, ranging from nano-objects close to ideal quantum wells or nanowires [56–58] to less characteristic systems in which one or two dimensions are smaller than the exciton Bohr radius, a_X, but the others are larger without being able to consider them infinite [17,59–61]. Being able to finely exploit the properties of anisotropic morphologies thus becomes a challenge: anisotropy might be used to control the polarization [62] or the directionality of the emitted light [63]. It also directly pilots the optical band-gap value and the EFS. In the past Nestoklon and coworkers [64] were the first authors to address the question of the role played by the shape anisotropy in the exciton bright-states splittings of cubic phase NCs. Ben Aich and coworkers [53] completed this work by incorporating, in their derivations, the crystal anisotropy and the confinement effects (through the long-range part of the e-h EI). However, a negative tetragonal crystal field term was used at that point instead of a positive contribution that is more consistent with crystallographic studies and recent DFT calculations [65]. These early studies have allowed to gain insights into the understanding of the fundamental excitonic properties, like the magneto-optical responses or the lifting, at zero-B field, of degeneracies in the EFS that cannot be explained on the basis of phase symmetry arguments exclusively.

The aim of the present work is to investigate the interplay of shape and crystal anisotropy, dielectric effects and quantum confinement on the EFS splittings focusing our attention on inorganic halide perovskite NCs with anisotropic morphologies that we cannot consider as ideal models of 2D or 1D systems. The dielectric constant discontinuity at the NC surface is the other strongly impacting feature at the microscopic level and has to be considered in a comprehensive way because it contributes at the millielectronvolt scale to the EFS. The influence of a dielectric contrast between the NC and its host was studied by Gupalov and Ivchenko [66], who considered spherical CdSe NCs and deduced a corrective coefficient to the long-range EI. This strategy was recently replicated in spherical halide perovskite NCs with the same corrective factor used to describe the EFS of cubic-shaped systems [55] leading to an overestimation of the long-range EI contribution to the exciton energy. Here, the description of the dielectric effects will be done in the image charges formalism, considering actual cubic/parallelepiped shapes without referring to the spherical symmetry like in previous studies [55,66].

In this work, we calculate the whole e-h EI interaction taking into account the short-range (analytic part) and the long-range (nonanalytic part) contributions. Additionally we explore how the shape anisotropy (by changing the NCs aspect ratio) influences the structure and ordering of the excitonic fine structure levels as well as their energy separation. This is done by considering the phase structures that are characteristic of perovskite materials (starting from the higher symmetric one, cubic—O_h—and going to lower symmetry structures like the tetragonal D_{4h} or orthorhombic D_{2h} ones) and simulating shape elongation/contraction along the relevant directions: (i) deformation along either one of the x, y, or z directions in the cubic phase and,(ii) deformation along the z direction (or "high symmetry" **c** axis) in the uniaxial tetragonal phase [43,55,65], but also along the y axis (i.e., in the plane orthogonal to **c**) or both.

Let us note that the assignment of a structural phase to a 0D system as temperature changes remains a tricky task. Regarding the case of $CsPbBr_3$ NCs, orthorhombic and tetragonal systems unambiguously coexist at cryogenic temperature [45,46] while there is still an important dispersions in the literature results in room-temperature characterization that sees each of the structure as plausible [60,67]. In the context, the cubic and tetragonal lattices thus remain important references as they present the highest degrees of symmetry and can be entirely and reliably parametrized in the method—$\mathbf{k}\cdot\mathbf{p}$ + effective mass approximation (EMA)—that is used to determine the EFS. By this way, analytic expressions are given for the EFS energies. In contrast, absolute predictions for the orthorhombic structure are more complex and depends on still unknown experimental parameters (like the crystal field amplitude); here a semiqualitative approach is thus used to describe the EFS dependence on the NC aspect ratio, within the hypothesis that the orthorhombic structure causes only slight perturbations in the parameters associated to the tetragonal configuration (see the discussion section).

We should emphasize that the continuum states method (parametrization of a $\mathbf{k}\cdot\mathbf{p}$ Hamiltonian in the EMA) that is used here is a good compromise to address systems that consist of a large number of atoms (several 10^4 typically for the NC itself, without considering the capping ligands that define the dielectric environment). This approach fills the gap left by many body perturbation methods (like the GW + Bethe-Salpeter formalism) capable to finely describe excitonic properties in low dimension systems made of a few hundreds of atoms or extended systems accommodating periodic boundary conditions [68,69] and atomistic methods, also competitive in systems composed of a smaller number of atoms [70–72]. For large NCs, a tight-binding calculation is an alternative method to estimate the e-h EI, as recently shown in lead chalcogenide NCs [73].

Moreover, the numerous studies comparing the performances of EMA based techniques and the *ab initio* (or atomistic) ones also agree on the range of validity that should be considered for the $\mathbf{k}\cdot\mathbf{p}$+ EMA method to keep reliable and performant in its predictions. A close inspection of the most significant works addressing colloidal NCs allows to extract a general criterion for a large panel of materials and exciton Bohr radius (a_X) [70,73–75], ranging from CdS (a_X = 2.8 nm) to PbS (a_X = 18 nm), under the form $\Xi > 2a_X$, where Ξ is a characteristic size parameter (diameter, edge length etc), meaning roughly that the confinement regime should not go beyond the intermediate one. We emphasize that the present study considers NCs for which the criterion is fully satisfied.

The manuscript is organized as follows. In Sec. II, we present the theoretical methodology used to compute the different splittings involved in the excitonic fine structure. We develop a variational approach to calculate the exchange interaction in NCs having cuboid shape taking into account the effects of quantum and dielectric confinements. In Sec. III, we discuss in detail the role of the shape anisotropy and dielectric contrast in the ordering of excitonic levels and their energetic splittings. We apply the model to $CsPbBr_3$ NCs which size domain covers the intermediate confinement regime and for all of the structural phases that may be encountered. We conclude in Sec. IV.

II. THEORETICAL METHODOLOGY

A. Bulk parameters

We propose a modeling of the electronic and excitonic properties of $CsPbBr_3$ NCs having cubic and tetragonal crystal symmetries. For this purpose, we first approximate the lattice as tetragonal and calculate band parameters for bulk perovskite compounds, $CsPbX_3$ ($X = Br, I, Cl$).

In Ref. [76], we adopted a 40-band $\mathbf{k}\cdot\mathbf{p}$ model [77,78] for the simple cubic structure for which the point group is O_h, in order to reproduce the energy band structure of cubic $CsPbX_3$ (see Fig. S9 in electronic supplementary information of Ref. [76]).

In the supplementary information of Ref. [79], we provide the physical parameters of tetragonal $CsPbX_3$ ($X = Br, I, Cl$) deduced from the 16-band $\mathbf{k}\cdot\mathbf{p}$ model [24].

The basic parameters for the different crystal symmetries that were used to calculate the band-edge excitons of $CsPbBr_3$ NCs are listed in Table I. The band-gap energies are obtained using the experimental data in Ref. [80]. The $\mathbf{k}\cdot\mathbf{p}$ method estimates the fundamental parameters [76,79], including the spin-orbit coupling Δ_C, tetragonal crystal field T, phase angle θ, and the Kane energies [E_{P_S} in cubic phase, ($E_{P_{S,\rho}}$, $E_{P_{S,z}}$) in tetragonal phase]. We fixed for ϵ_1, ϵ_X, and a_X, the same values in all the symmetries [81,82], in the lack of experimental measurements.

B. Electronic wave functions and electrons states in nanocrystals

In NCs when strong confinement and infinite wells are considered in the three directions x, y, and z, one can write the envelope wave function of the carrier ground state as

$$\phi_\ell(\mathbf{r}_\ell) = \sqrt{\frac{2^3}{L_xL_yL_z}}\cos\left(\frac{\pi x_\ell}{L_x}\right)\cos\left(\frac{\pi y_\ell}{L_y}\right)\cos\left(\frac{\pi z_\ell}{L_z}\right), \quad (1)$$

in which L_x, L_y, and L_z are the dimensions of the rectangular parallelepiped-shaped NC. We then write the carrier confinement energy as $E_\ell = (\hbar^2\pi^2/2m_\ell)(n_x^2/L_x^2 + n_y^2/L_y^2 + n_z^2/L_z^2)$, m_ℓ being the effective mass of carrier ℓ ($\ell = e, h$). n_x, n_y, and n_z are the quantification integer numbers along x, y, and z directions, respectively. The ground state corresponds to $n_x = n_y = n_z = 1$. After having described independent particles with single band effective mass approach, we then consider the problem of excitons. In absence of Coulomb interaction, an e-h pair system can be described with the following effective mass Hamiltonian $\mathcal{H}_0 = \sum_{\ell=e,h}[\mathcal{T}_\ell + \mathcal{V}_\ell^{\text{conf}}(\mathbf{r}_\ell)] + E_g$, where $\mathcal{T}_\ell = p_\ell^2/2m_\ell$ is the kinetic contribution of carrier ℓ, p_ℓ being the momentum operators of particle ℓ. We take the spatial confinement potential as $\mathcal{V}_\ell^{\text{conf}} = 0$ inside the NC and $\mathcal{V}_\ell^{\text{conf}} = +\infty$ outside. E_g is the bulk band-gap energy and $\mathbf{r}_\ell$ the position vector of carrier ℓ. The ground state energy of the e-h pair system is $\mathcal{E}_0 = E_g + (\hbar^2\pi^2/2\mu)(1/L_x^2 + 1/L_y^2 + 1/L_z^2)$, where $\mu^{-1} = m_e^{-1} + m_h^{-1}$ with μ the reduced exciton mass.

1. Coulomb interaction and dielectric effect

We resort to the method of image charges, a well-established procedure in electrostatics, to reproduce the electric field created by polarization charges due to the dielectric mismatch [83,84]. In this picture, an exciton in a NC can be described by the following Hamiltonian:

$$\mathcal{H} = \sum_{\ell=e,h}\left[\mathcal{T}_\ell + \mathcal{V}_\ell^{\text{conf}}(\mathbf{r}_\ell) + \mathcal{V}_\ell^{\text{self}}(\mathbf{r}_\ell)\right] + \mathcal{V}_C(\mathbf{r}_e, \mathbf{r}_h) + E_g, \quad (2)$$

where $\mathcal{V}_C(\mathbf{r}_e, \mathbf{r}_h)$ is a "corrected" direct e-h Coulomb contribution and $\mathcal{V}_\ell^{\text{self}}$ (the self-energy potential) is a term that has to be added in order to ensure the global consistency of the electrostatic problem as the discontinuous medium is replaced by a uniform environment characterized by a modified effective permittivity (see below).

TABLE I. Summary of bulk parameters used to calculate the $CsPbBr_3$ nanocrystals fine structure exciton states. E_g denotes the bulk band-gap energy, Δ_C the spin-orbit coupling, T the tetragonal crystal field, θ the phase angle defined as $\tan 2\theta = (2\sqrt{2}\Delta_C)/(\Delta_C - 3T)$ (with $0 < \theta < \pi/2$), ϵ_1 the dielectric constant inside the NC, ϵ_X the dielectric constant at the exciton resonance, a_X the exciton Bohr radius. E_{P_S} represents the Kane energy in cubic phase and related to the matrix element P_S by $E_{P_S} = (2m_0/\hbar^2)|P_S|^2$. $(E_{P_{S,\rho}}, E_{P_{S,z}})$ are the Kane energies in tetragonal phase and defined as $E_{P_{S,i}} = (2m_0/\hbar^2)|P_{S,i}|^2$ $(i = \rho, z)$.

Band parameters of $CsPbBr_3$										
	E_g (eV)	Δ_C (eV)	T (meV)	θ (°)	ϵ_1	ϵ_X	a_X (nm)	E_{P_S} (eV)	$E_{P_{S,\rho}}$ (eV)	$E_{P_{S,z}}$ (eV)
cubic	2.38[a]	1.39[b]	0	35.26	7.3[d]	4.45[e]	3.07[d]	28.41[b]		
tetragonal	2.37[a]	1.49[c]	147[c]	40.4[c]	7.3[d]	4.45[e]	3.07[d]		16.8[c]	15.65[c]

[a]Reference [80].
[b]Reference [76].
[c]Reference [79].
[d]Reference [81].
[e]Reference [82].

In NCs having edge lengths (L_x, L_y, L_z), we can model the self-energy potential due to the image charges as

$$\mathcal{V}_\ell^{\text{self}} = \frac{e^2}{4\pi\epsilon_0\epsilon_1} \sum_{\substack{m=-\infty \\ m\neq 0}}^{+\infty} \sum_{\substack{n=-\infty \\ n\neq 0}}^{+\infty} \sum_{\substack{p=-\infty \\ p\neq 0}}^{+\infty} \times \frac{1}{2} \frac{\eta^{|m|+|n|+|p|}}{\sqrt{(x_\ell - x_{\ell m})^2 + (y_\ell - y_{\ell n})^2 + (z_\ell - z_{\ell p})^2}} \quad (3)$$

in which $\eta = (\epsilon_1 - \epsilon_2)/(\epsilon_1 + \epsilon_2)$, η being the dielectric contrast. We denote by ϵ_1 and ϵ_2 the dielectric constants inside and outside the NCs, respectively. $x_{\ell m} = (-1)^m x_\ell + mL_x$, $y_{\ell n} = (-1)^n y_\ell + nL_y$, $z_{\ell p} = (-1)^p z_\ell + pL_z$, recalling that $\ell = e, h$.

Taking into account the modification due to the dielectric mismatch, the e-h Coulomb interaction is given by

$$\mathcal{V}_C = -\frac{e^2}{4\pi\epsilon_0\epsilon_1} \sum_{m=-\infty}^{+\infty} \sum_{n=-\infty}^{+\infty} \sum_{p=-\infty}^{+\infty} \times \frac{\eta^{|m|+|n|+|p|}}{\sqrt{(x_e - x_{hm})^2 + (y_e - y_{hn})^2 + (z_e - z_{hp})^2}}. \quad (4)$$

Taking $\eta = 0$, we find the usual expression of the e-h Coulomb interaction $\mathcal{V}_C(\mathbf{r}_e, \mathbf{r}_h) = -\frac{e^2}{4\pi\epsilon_0\epsilon_1} \frac{1}{|\mathbf{r}_e - \mathbf{r}_h|}$.

The Hamiltonian $\mathcal{H}$ can be solved by using a variational approach and the following exciton trial function:

$$\Psi(\mathbf{r}_e, \mathbf{r}_h) = \mathcal{N}(a)\left[\exp\left(-\frac{1}{a}\sqrt{(x_e - x_h)^2 + (y_e - y_h)^2 + (z_e - z_h)^2}\right)\right] \times \phi_e(\mathbf{r}_e)\phi_h(\mathbf{r}_h). \quad (5)$$

Due to the 3D symmetry of the potentials $\mathcal{V}_\ell^{\text{self}}$ and $\mathcal{V}_C$, the energy contributions $\langle\Psi|\mathcal{V}_\ell^{\text{self}}|\Psi\rangle$ and $\langle\Psi|\mathcal{V}_C|\Psi\rangle$ are sixfold integrals and solving the variational problem is time consuming. To reduce the computing time, we have only considered the image charges along the three symmetry axes x, y, z (this includes the nearest image charges for the six NC faces). This reduces the integral multiplicity to quadruple.

It is finally important to comment about the infinite barrier approximation that is made in this work (through $\mathcal{V}_\ell^{\text{conf}} = +\infty$ outside the NC). In the infinite barrier regime, the confinement energy of the carriers (that have nearly the same mass [85]) is estimated to be (0.06 eV) in NCs having edge lengths poorly varying around the central value, $\langle L\rangle = L_x = L_y = L_z = 8$ nm (see below). The confinement energy thus remains small compared to the actual confinement barrier height that was estimated to be around 1 eV (electrons) and 3 eV (holes) in NCs capped with classical ligands like oleic acid or oleyamine [86]. This justifies the infinite barrier choice that, to the best of our knowledge, has been so far systematically used to model perovskite nanosystems.

2. Electron-hole exchange interaction

Initially, the theory of e-h EI was investigated in bulk semiconductors by Bir and Pikus [87,88] and Denisov and Makarov [89]. Later, the interest for e-h EI has involved also III-V and II-VI semiconductors low dimension systems, more precisely quantum wells [90,91] or quantum dots [50,51,74,92,93]. Recently, the e-h EI has been computed in fully inorganic and hybrid halide perovskites NCs [24,46,49,53,55,65].

To model this interaction, one includes both long-range (LR) exchange (also named non analytic) and the analytic short-range (SR) exchange contributions. In zinc-blende compounds, the EFS is organized into two doublets, a bright-doublet and dark-doublet. Both LR and SR interactions play a role to the dark-bright and bright-bright splittings with disparate orders of magnitude [94]. In halide perovskite semiconductors, only one single dark state exists, but three bright states contribute to the EFS. The splittings within the bright triplet and between dark-bright states contain LR and SR contributions with comparable orders of magnitude [24,55].

The charged carrier states involved in the formation of the lowest energy excitonic pair states are a conduction band electron $|j_z = 1/2, j_z^e = \pm 1/2\rangle$ and a valence band hole $|j_z = 1/2, j_z^h = \pm 1/2\rangle$. Four exciton states are generated: the triplet states with an angular momentum $j = 1$ and z components of angular momentum $j_z = 0, \pm 1$, which are bright exciton states and will be denoted as $|+1\rangle, |0_B\rangle, |-1\rangle$, and a singlet state with an angular momentum $j = 0$ $(j_z = 0)$, which is a dark exciton state and will be denoted as $|0_D\rangle$. These four

excitonic states can be written as

$$|0_D\rangle = \frac{1}{\sqrt{2}}\left[\left|+\frac{1}{2},-\frac{1}{2}\right\rangle - \left|-\frac{1}{2},+\frac{1}{2}\right\rangle\right]$$
$$|0_B\rangle = \frac{1}{\sqrt{2}}\left[\left|+\frac{1}{2},-\frac{1}{2}\right\rangle + \left|-\frac{1}{2},+\frac{1}{2}\right\rangle\right]$$
$$|+1\rangle = \left|+\frac{1}{2},+\frac{1}{2}\right\rangle;\ |-1\rangle = \left|-\frac{1}{2},-\frac{1}{2}\right\rangle. \quad (6)$$

To derive the matrix representation of the e-h EI SR contribution $\mathcal{H}^{\rm SR}$, we adopt SR interaction as a spin-dependent contact interaction [95]

$$\mathcal{H}^{\rm SR} = \tfrac{1}{2}C(\mathfrak{I} - \boldsymbol{\sigma_e}.\boldsymbol{\sigma}_h)\delta(\mathbf{r}_e - \mathbf{r}_h) \quad (7)$$

in which C is the SR exchange constant, deduced from experimental data in Ref. [24] ($C = 107.6$ meV nm^3) and agrees very well with the theoretical values ($C =$ 92.2–105.7 meV nm^3) obtained by DFT in Ref. [65]. In Eq. (7), $\mathfrak{I}$ is the 4×4 unitary matrix, $\boldsymbol{\sigma}_e$ and $\boldsymbol{\sigma}_h$ are the Pauli operators describing the electron and hole spin.

In the basis $\{|+1\rangle, |-1\rangle, |0_B\rangle; |0_D\rangle\}$, the $\mathcal{H}^{\rm SR}$ matrix takes the form

$$\mathcal{H}^{\rm SR} = \frac{3}{2}\Delta_{\rm SR}\pi a_X^3\mathcal{K}\begin{bmatrix} \alpha^2+\beta^2 & -\alpha^2+\beta^2 & 0 & 0 \\ -\alpha^2+\beta^2 & \alpha^2+\beta^2 & 0 & 0 \\ 0 & 0 & 2\gamma^2 & 0 \\ 0 & 0 & 0 & 0 \end{bmatrix}, \quad (8)$$

where $\Delta_{\rm SR} = (2C/3\pi a_X^3)$, a_X being the exciton Bohr radius, and $\mathcal{K} = \int_V |\Psi(\mathbf{r},\mathbf{r})|^2 d\mathbf{r}$. From the $\Psi(\mathbf{r},\mathbf{r})$ expression, we get $\mathcal{K} = (27/8)(|\mathcal{N}(a)|^2/L_xL_yL_z)$. In a low symmetry phase, the coefficients (α,β,γ) will depend on the orthorhombic crystal fields and they are given explicitly in Ref. [46]. In the tetragonal phase, $\alpha^2 = \beta^2 = (\cos^2\theta)/2$ and $\gamma^2 = \sin^2\theta$, where $\tan 2\theta = (2\sqrt{2}\Delta_C)/(\Delta_C - 3T)$ (with $0 < \theta < \pi/2$). Δ_C being the spin-orbit coupling in conduction band and T is the tetragonal crystal field. In the cubic phase, there is no crystal-field and $\alpha^2 = \beta^2 = \gamma^2 = 1/3$.

The LR and SR parts of the EI own the same symmetry so, using $\{|+1\rangle, |-1\rangle, |0_B\rangle; |0_D\rangle\}$ as the basis, the following matrix representation is obtained

$$\mathcal{H}^{\rm LR} = \begin{bmatrix} \Sigma_d & \Sigma_{od} & 0 & 0 \\ \Sigma_{od} & \Sigma_d & 0 & 0 \\ 0 & 0 & \Sigma_z & 0 \\ 0 & 0 & 0 & 0 \end{bmatrix}. \quad (9)$$

The detailed derivation of the matrix elements of $\mathcal{H}^{\rm LR}$ is given in Appendix A and their expressions are given and discussed in the next section.

3. Shape anisotropy and dielectric effects

The following matrix elements are obtained

$$\Sigma_d = \left[\alpha^2 E_{P_{S,x}} I_x + \beta^2 E_{P_{S,y}} I_y\right]\Lambda\pi^9\left(\frac{\pi a_X^3}{L_x^3}\right)\left(\frac{3|\mathcal{N}(a)|^2}{rs}\right)$$
$$\Sigma_{od} = \left[-\alpha^2 E_{P_{S,x}} I_x + \beta^2 E_{P_{S,y}} I_y\right]\Lambda\pi^9\left(\frac{\pi a_X^3}{L_x^3}\right)\left(\frac{3|\mathcal{N}(a)|^2}{rs}\right)$$
$$\Sigma_z = 2\gamma^2 E_{P_{S,z}} I_z \Lambda\pi^9\left(\frac{\pi a_X^3}{L_x^3}\right)\left(\frac{3|\mathcal{N}(a)|^2}{rs}\right), \quad (10)$$

with $\Lambda = (1/3E_g^2)(\hbar^2/2m_0)(e^2/\epsilon_0\epsilon_X)(1/\pi a_x^3)$. The NC anisotropy is parametrized by the coefficients $r = L_y/L_x$ and $s = L_z/L_x$. $E_{P_{S,j}} = (2m_0/\hbar^2)P_{S,j}^2 (j = x,y,z)$ are the related energies to the nonzero matrix elements of the momentum operator $\mathbf{p}$, $P_{S,j}$, according to D_{2h} point group symmetry. In the following, for simplicity, in Eq. (10), we assume $E_{P_{S,x}} = E_{P_{S,y}} = E_{P_{S,\rho}}$, noting that this assumption is justified in cubic and tetragonal structures.

The integrals I_j are expressed as

$$I_x = \int d\mathbf{u}\frac{r^2s^2u_x^2}{r^2s^2u_x^2 + s^2u_y^2 + r^2u_z^2}\frac{\sin^2 u_x}{u_x^2\left(u_x^2-\pi^2\right)^2}\frac{\sin^2 u_y}{u_y^2\left(u_y^2-\pi^2\right)^2}\frac{\sin^2 u_z}{u_z^2\left(u_z^2-\pi^2\right)^2}d_+(u_x)d_-(u_y)d_-(u_z)$$
$$I_y = \int d\mathbf{u}\frac{s^2u_y^2}{r^2s^2u_x^2 + s^2u_y^2 + r^2u_z^2}\frac{\sin^2 u_x}{u_x^2\left(u_x^2-\pi^2\right)^2}\frac{\sin^2 u_y}{u_y^2\left(u_y^2-\pi^2\right)^2}\frac{\sin^2 u_z}{u_z^2\left(u_z^2-\pi^2\right)^2}d_-(u_x)d_+(u_y)d_-(u_z)$$
$$I_z = \int d\mathbf{u}\frac{r^2u_z^2}{r^2s^2u_x^2 + s^2u_y^2 + r^2u_z^2}\frac{\sin^2 u_x}{u_x^2\left(u_x^2-\pi^2\right)^2}\frac{\sin^2 u_y}{u_y^2\left(u_y^2-\pi^2\right)^2}\frac{\sin^2 u_z}{u_z^2\left(u_z^2-\pi^2\right)^2}d_-(u_x)d_-(u_y)d_+(u_z), \quad (11)$$

in which $d_\pm(u) = (1-\eta^2)/(1+\eta^2 \pm 2\eta\cos(2u))$ and $\eta = \frac{\epsilon_1-\epsilon_2}{\epsilon_1+\epsilon_2}$. In absence of dielectric mismatch, that is, when the ratio of the dielectric contrast is $\eta = 0$, one has $d_\pm(u) = 1$. In the following, we will develop a comprehensive analysis of dielectric effects on the EFS. For this purpose, we compare the results including or not such effects by conducting the present calculation for three values of the outside dielectric constant, namely, $\epsilon_2 = 1$ (vacuum or air; red curves), $\epsilon_2 = 2$ (glass, common organic solvents for colloidal NCs, ligands; green curves), and $\epsilon_2 = \epsilon_1 = 7.3$ (in absence of dielectric mismatch; blue curves). It is then possible to calculate the excitonic eigenvalues and eigenstates of the exchange Hamiltonian $\mathcal{H}_{\rm exch} = (\mathcal{H}^{\rm SR} + \mathcal{H}^{\rm LR})$. After $\mathcal{H}_{\rm exch}$ diagonalization procedure, we obtain

$$E_{|X\rangle} = [2\Lambda_x E_{P_{S,\rho}} + 3\Delta_{\rm SR}]\mathcal{K}\alpha^2\pi a_X^3 \ ; |X\rangle = \frac{1}{\sqrt{2}}[|+1\rangle - |-1\rangle]$$
$$E_{|Y\rangle} = \left[2\Lambda_y E_{P_{S,\rho}} + 3\Delta_{\rm SR}\right]\mathcal{K}\beta^2\pi a_X^3 \ ; |Y\rangle = \frac{1}{\sqrt{2}}[|+1\rangle + |-1\rangle]$$

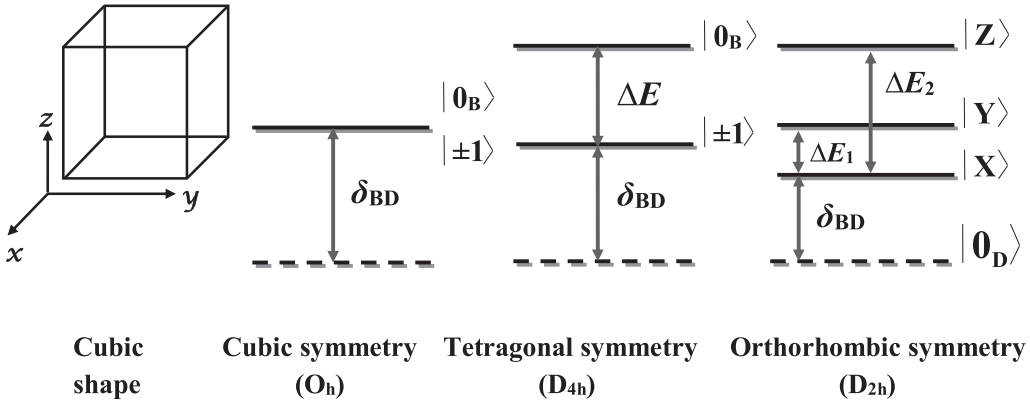

FIG. 1. Exciton fine structures (EFSs) for nanocrystals in absence of shape anisotropy are shown schematically for the cases with cubic (O_h as point group), tetragonal (D_{4h} as point group), and orthorhombic crystal symmetry (D_{2h} as point group). The three bright states are fully degenerate in cubic symmetry.

$$E_{|Z\rangle} = [2\Lambda_z E_{P_{S,z}} + 3\Delta_{SR}]\mathcal{K}\gamma^2\pi a_X^3 \quad ; |Z\rangle = |0_B\rangle$$
$$E_D = 0 \ ; |0_D\rangle, \tag{12}$$

where $\Lambda_l = \frac{8\pi^9}{9}\Lambda I_l$ $(l = x, y, z)$. Note that $E_{|\Theta\rangle}$ designs an exciton associated to a transition linearly polarized along the Θ direction.

In absence of anisotropy ($r = s = 1$) $I_x = I_y = I_z$, one obtains a triply degenerate bright-exciton state for a cubic crystal phase ($\alpha^2 = \beta^2 = \gamma^2 = \frac{1}{3}$; $E_{P_{S,\rho}} = E_{P_{S,z}} = E_{P_S}$), a doublet for the tetragonal phase ($\alpha = \beta \neq \gamma$; $E_{P_{S,\rho}} \neq E_{P_{S,z}}$) with $\mathbf{z} \parallel \mathbf{c}$ axis of D_{4h} symmetry and a triplet in the orthorhombic phase ($\alpha \neq \beta \neq \gamma$; $E_{P_{S,x}} \neq E_{P_{S,y}} \neq E_{P_{S,z}}$) (see Fig. 1 where the splittings definitions are given).

To be able to gain insights into the impact of the dielectric confinement with regard to the actual NC shape (cubic versus spherical) we examine the case of an isotropic NC ($r = s = 1$). Then, the integrals in Eq. (11) reduce to a unique integral $I(\eta)$ depending only on $\eta = (\epsilon_1 - \epsilon_2)/(\epsilon_1 + \epsilon_2)$. We define the renormalized coefficient $\mathcal{C}_{\rm cub} = \frac{I(\eta)}{I(0)}$ with $I(0) = \frac{9}{8\pi^9}$, the value of I when there is no dielectric contrast. Importantly, in absence of shape anisotropy $\mathcal{C}_{\rm cub}$ appears to be the prefactor in the LR contribution of the EI. In Fig. 2, $\mathcal{C}_{\rm cub}$ is thus compared to $\mathcal{C}_{\rm sph}$, the equivalent coefficient, determined for a spherical NC, resorting in the same manner to the image charges formalism [66]. $\mathcal{C}_{\rm sph}$ writes

$$\mathcal{C}_{\rm sph} = 1 + \frac{12}{\pi^2}\frac{\epsilon_1 - \epsilon_2}{\epsilon_1 + 2\epsilon_2} = 1 + \frac{12}{\pi^2}\frac{2\eta}{3 - \eta} \tag{13}$$

and is always larger than $\mathcal{C}_{\rm cub}$ as η varies from its minimal value, $\eta = 0$ (for $\epsilon_1 = \epsilon_2$), to its maximal value, $\eta = \eta_{\rm max} \simeq 0.76$ (for $\epsilon_1 = 7.3$ and $\epsilon_2 = 1$). Both coefficients are increasing functions of the dielectric contrast, in a similar way, with a ratio close to 2/3 between the dielectric contributions $(\mathcal{C}_{\rm cub} - 1)$ and $(\mathcal{C}_{\rm sph} - 1)$. At $\eta = \eta_{\rm max}$, $\mathcal{C}_{\rm sph}$ is about 20% larger than $\mathcal{C}_{\rm cub}$ in $CsPbBr_3$ compounds. As a consequence, it should be pointed out that reaching finer energetics for the EFS requires to adjust the electrostatic issue to the geometry specificities. It is clearly evidenced here that using $\mathcal{C}_{\rm sph}$ to capture the dielectric mismatch effects in cubic shape NCs, like in Ref. [55], is at the origin of a sizable overestimation of the long-range EI contribution to the exciton energy.

Figure 3 shows the dependence of the calculated exchange integrals, $I_l(l = x, y, z)$, as a function of the anisotropy parameter r. In Fig. 3(a) ($s = 1$), we denote $I_\perp = I_x = I_z$ (solid lines) and $I_{//} = I_y$ (dashed lines). At $r = 1$ ($L_x = L_y = L_z$), all the directions are equivalent (perfect isotropy) and $I_{//} = I_\perp$ for a given value of ϵ_2. $I_\perp$ is an increasing function of the anisotropy r, while $I_{//}$ is a decreasing function. Each integral I_l is directly related to the NC length L_l so that (i) we elongate the NC along Oy direction for $r > 1$, $I_{//} < I_\perp$ ($L_y > L_x = L_z$ or $L_{//} > L_\perp$); and (ii) we contract the NC along Oy direction for $r < 1$, $I_{//} > I_\perp$ ($L_{//} < L_\perp$). Due to the functions $d_\pm(u) \neq 1$ in Eq. (11), in presence of a dielectric mismatch ($\epsilon_2 < \epsilon_1$),

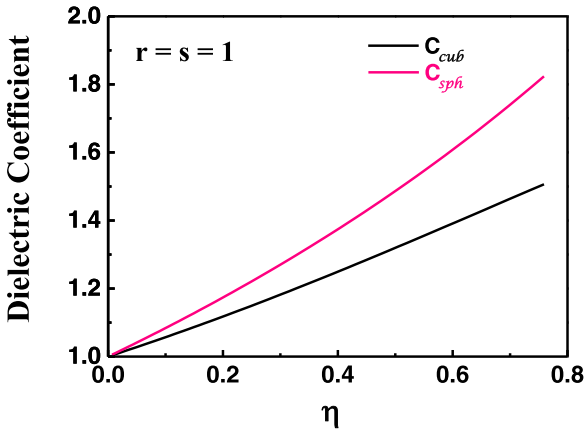

FIG. 2. Case of isotropic NC: effect of dielectric contrast on the corrective factors, $\mathcal{C}_{\rm sph}$ and $\mathcal{C}_{\rm cub}$, of the long-range exchange interaction due to dielectric contrast for an isotropic NC. $\mathcal{C}_{\rm sph}$ [Eq. (13)] is for a spherical NC, and $\mathcal{C}_{\rm cub}$, is calculated within the image charges formalism when considering a cuboid shaped NC. The factors are plotted as a function of $\eta = (\epsilon_1 - \epsilon_2)/(\epsilon_1 + \epsilon_2)$.

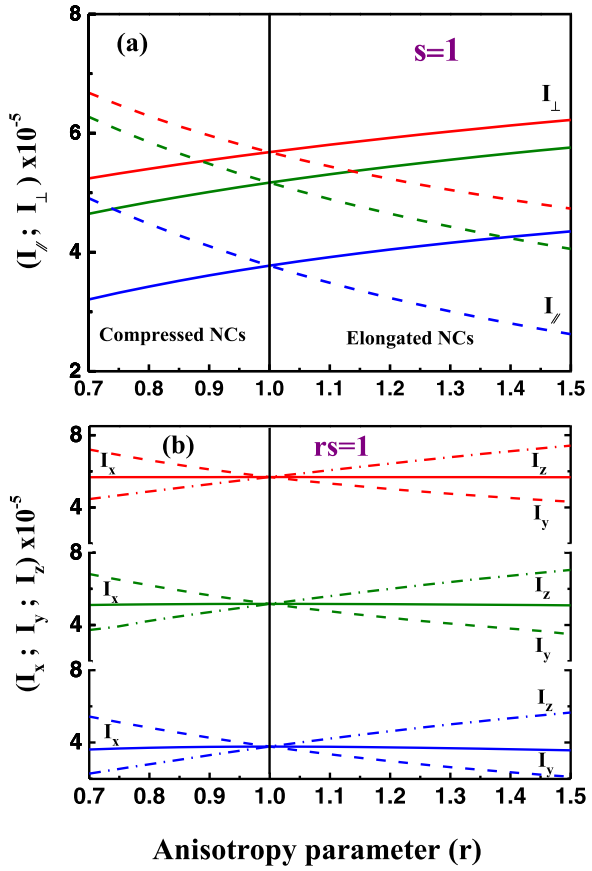

FIG. 3. (a) Dependence of the exchange integrals with the anisotropy parameter r while $s = 1$. For $r > 1$ ($r < 1$), the NC size along one direction is elongated (reduced). (b) Exchange integrals as a function of the anisotropy parameter r while $rs = 1$. Different dielectric contrasts are considered (blue curves, outside dielectric constant $\epsilon_2 = 7.3$; green, $\epsilon_2 = 2$; red, $\epsilon_2 = 1$).

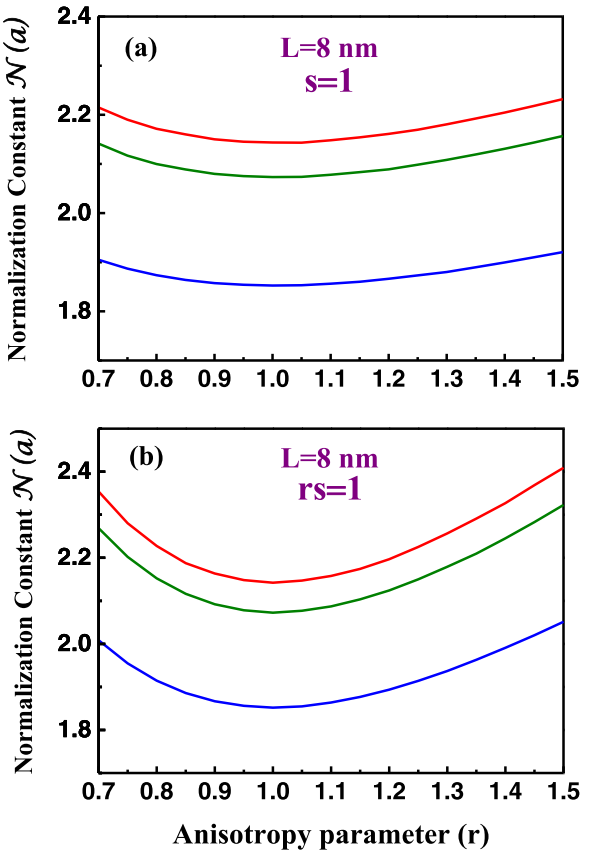

FIG. 4. Effect of the shape anisotropy and dielectric contrast on the normalization factor, $\mathcal{N}(a)$, of the trial function Eq. (5). Different outside dielectric constants are considered (blue curves for $\epsilon_2 = 7.3$; green for $\epsilon_2 = 2$; red for $\epsilon_2 = 1$). (a) $\mathcal{N}(a)$ as a function of r when elongating or reducing the NC size along a single direction. (b) $\mathcal{N}(a)$ vs r when assuming a shape distortion along two directions. The NC volume $V = L^3$ is kept constant ($L = 8$ nm).

the difference between the integrals $I_\perp$ and $I_{//}$ is very slightly decreased. The s dependence ($r = 1$), can be deduced with the changed relations $I_\perp = I_x = I_y$ and $I_{//} = I_z$.

Assuming a shape distortion along two directions, we set $r \neq 1$ and $rs = 1$. In this case, $I_x \neq I_y \neq I_z$ for $r \neq 1$. The r dependence of the integrals is shown in Fig. 3(b). The solid, dashed and dash-dotted lines correspond to I_x, I_y and I_z, respectively. Once again, the behavior of the integrals depends on the NC lengths, with $I_y < I_x < I_z$ for $L_y > L_x > L_z$ ($r > 1$), and a reverse order for $r < 1$. In the presence of a dielectric mismatch and for a given value of ϵ_2, the integral I_x is almost invariant while a significant effect can be observed for I_y and I_z with an increase in their difference as r shifts away from 1. Finally, we discuss the effect of the shape anisotropy and the dielectric contrast on the wave function coefficient $\mathcal{N}(a)$ [see Eq. (5)]. As seen in Fig. 4, $\mathcal{N}(a)$ increases significantly with the dielectric contrast in both cases $r = 1$ or $rs = 1$, while it is only poorly dependent of the shape anisotropy as long as the latter remains weak.

III. RESULTS AND DISCUSSION

In order to investigate how extrinsic factors might influence the EFS, we distinguished essentially two ways to generate anisotropy (only cubic and tetragonal phases were considered in the present work). First, we increase or decrease the NC size along one direction only ($r \neq 1$ or $s \neq 1$), second we elongate or contract the NC along two directions (concomitant variation of r and s). Let us stress that both transformations are done while keeping the NC volume constant. Consequently, if we note ($V = L_x L_y L_z = L^3$), the dimensions read $L_x = (rs)^{-1/3} L$, $L_y = rL_x$, and $L_z = sL_x$; $rs = 1$ also comes as a supplementary constraint in the second "deformation scheme" to work with a constant volume. Then, we apply the general expressions providing the levels energy [Eq. (12)] to the case of $CsPbBr_3$.

A. Cubic phase (O_h symmetry)

In Fig. 5, $r = 1$ corresponds to a NC with a cubic shape $L_x = L_y = L_z = L$. As expected the exciton degeneracy is threefold; the bright state—dark state exciton splitting $\delta_{\rm BD}$ is written

$$\delta_{\rm BD} = \left[2\Lambda E_{P_S} + 3\Delta_{\rm SR}\right]\mathcal{K}\frac{\pi a_X^3}{3}. \tag{14}$$

The SR and LR parts of e-h EI contribute to this splitting and the splitting increases with decreasing NC size, L. For

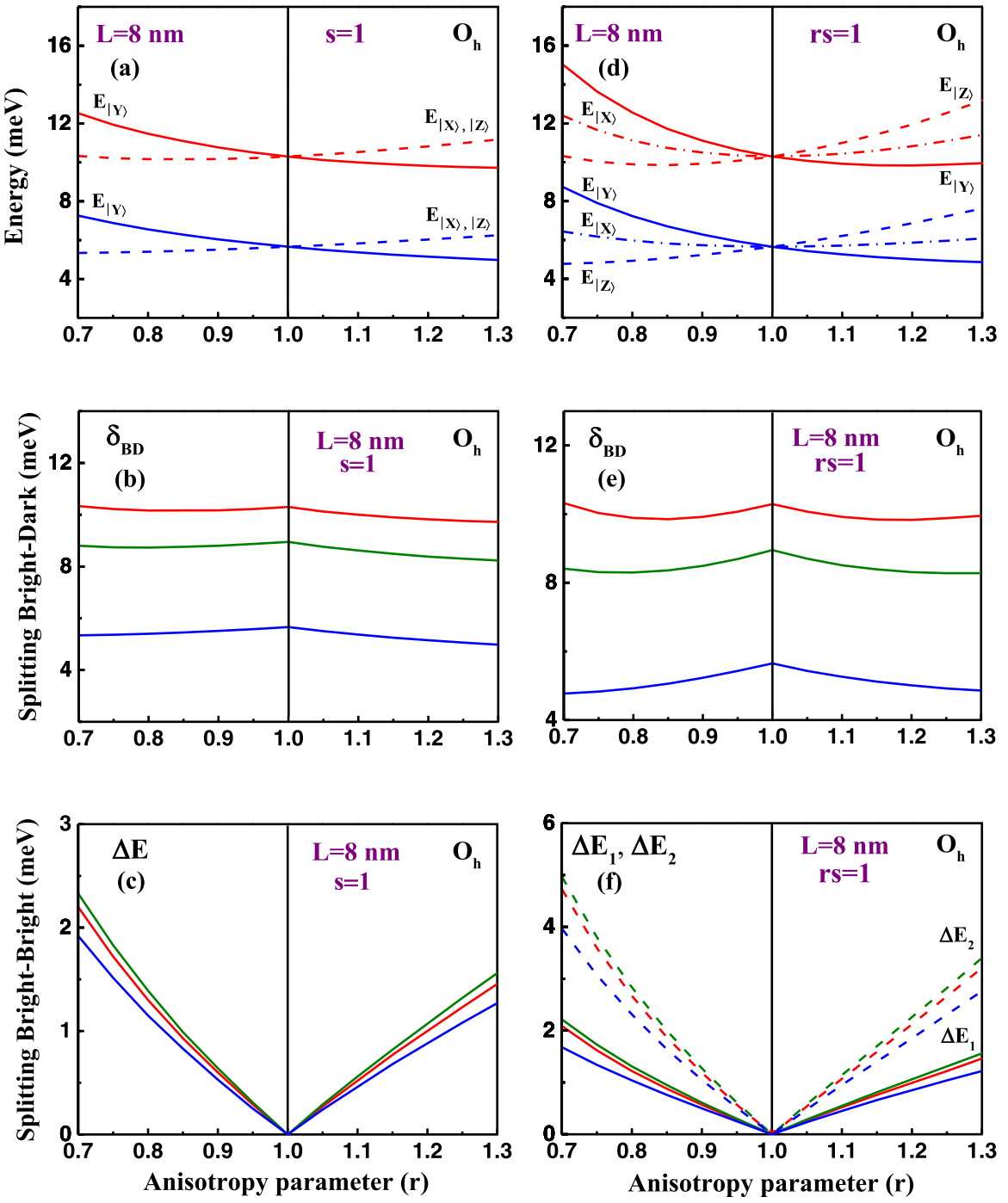

FIG. 5. Exciton fine structure of NCs with crystal phase O_h. Different dielectric contrasts are considered (blue color for $\epsilon_2 = 7.3$; green for $\epsilon_2 = 2$; red for $\epsilon_2 = 1$). (a) Bright states energies, (b) bright-dark splitting, δ_{BD}, and (c) bright-bright splitting, ΔE, when elongating or reducing the NC size along a single direction. (d) Bright states energies, (e) bright-dark splitting δ_{BD}, and (f) bright-bright splitting ΔE, calculated when assuming a shape distortion along two directions.

a given size the splitting increases with increasing dielectric contrast between the NC and the surrounding medium.

1. Shape anisotropy effect: $s = 1$ and $r \neq 1$

Figures 5(a)–5(c) show, for $L = 8$ nm, the results as a function of r values when $s = 1$. In this situation, we modify the NC aspect ratio in the Oy direction. The bright exciton triplet is then partially split in one singlet $E_{|Y\rangle}$ and one doublet $(E_{|X\rangle}, E_{|Z\rangle})$. The NC is elongated along the Oy direction when $r > 1$. Consequently, the state corresponding to the dipole along this direction is pushed to lower energy and the doubly degenerate states to higher energy. When $r < 1$, the situation is reversed and the doubly degenerate exciton states are found at lower energy.

The absolute value of the splitting between the bright singlet $E_{|Y\rangle}$ and doublet $(E_{|X\rangle}, E_{|Z\rangle})$ states is an increasing function of the anisotropy whatever $r < 1$ or $r > 1$. With

respect to the case without dielectric mismatch, for a given value of $r \neq 1$, the splitting slightly increases with the dielectric contrast [see Fig. 5(c)] and at the same time we note that $|\Delta E(\epsilon_2 = 2.0)| \gtrsim |\Delta E(\epsilon_2 = 1.0)|$.

On one hand, the δ_{BD} splitting [Fig. 5(b)] shows a weak dependence with the anisotropy level. On the other hand, an important result is that δ_{BD} is more sensitive to the dielectric mismatch: it is multiplied by a factor $\simeq 2$ between the no contrast-strong contrast situations.

An equivalent discussion can be written when $r = 1$ and $s \neq 1$ by swapping Oy and Oz directions.

2. Shape anisotropy effects: rs = 1

In Figs. 5(d)–5(f), we now keep $rs = 1$ ($L = 8$ nm), and the value of the anisotropy parameter r is varied, i.e., the deformations apply along two directions while still preserving the NC volume. For $r \neq 1$, three nondegenerate bright exciton states are revealed. Increasing r above 1 implies decreasing s: the contraction along Oz and the concerted elongation along Oy promote the $|Z\rangle$ level to the top and $E_{|Y\rangle}$ becomes the lowest energy value; $E_{|X\rangle}$ show moderate variations. Now, if $r < 1$ and $s > 1$, the main difference is the inversion in their position of the $|Z\rangle$ and $|Y\rangle$ levels.

The absolute values of ΔE_1 and ΔE_2 increase when the aspect ratio moves away from the maximum symmetry, $r = 1$ [see Fig. 5(f)] and for $0.8 < r < 1.2$, they are almost insensitive to the dielectric contrast. The increase is larger for $r = 0.7$ than for $r = 1.3$.

A quasi stationary evolution of the δ_{BD} splitting is also observed. The enhancement with the dielectric contrast is also strong as for the case $s = 1$.

B. Tetragonal phase (D_{4h} symmetry)

In the tetragonal phase, the excitonic states are defined by Eq. (12) when taking $\alpha^2 = \beta^2 = (\cos^2\theta)/2$ and $\gamma^2 = \sin^2\theta$. Three shape distortions are considered here; they are defined relatively to the "high symmetry" axis of the structure.

1. Shape anisotropy, r = 1

This case corresponds to an elongation of the NC size along the tetragonal axis of the crystal. Here, there are clear similarities with the case previously presented for the O_h crystal symmetry with $r = 1$ and $s \neq 1$.

As seen in Fig. 6(a), the EFS is composed of a singlet ($|Z\rangle$ state polarized along the **c** axis) and a degenerate doublet ($|X\rangle$, $|Y\rangle$ states) with an energy order that is maintained ($E_{|Z\rangle} > E_{|X\rangle,|Y\rangle}$) even if a relatively strong deformation is applied. In the following configurations, namely ($\epsilon_2 = 1$, $s = 2.085$) and ($\epsilon_2 = 7.3$, $s = 1.615$), we obtain a triply degenerate bright exciton state. A similar situation to the case $r = s = 1$ for O_h symmetry.

For a given dielectric contrast, δ_{BD} is a flat function of the s parameter. A more crucial aspect, for it should be easily connected to the experimental observables, is the significant decrease of the absolute δ_{BD} value when passing from the O_h to the D_{4h} symmetry ($\simeq -60\%$). For the sake of completeness, the splitting $\Delta E = E_{|Z\rangle} - E_{|X\rangle}$ until $s = 1.3$ is plotted in Fig. 6(c).

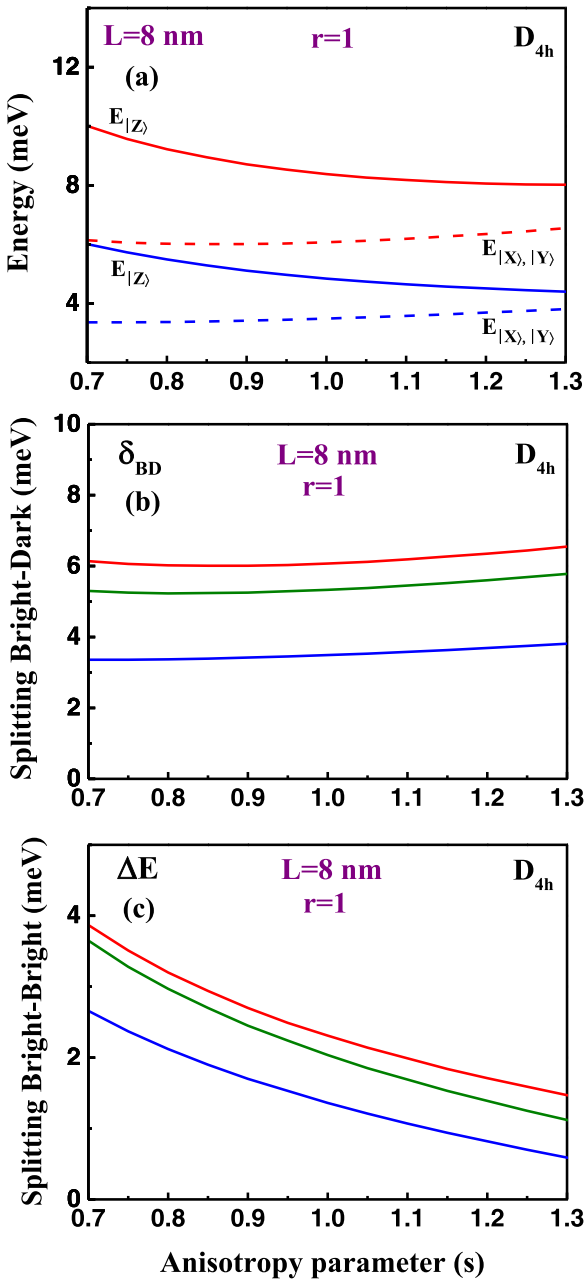

FIG. 6. Exciton fine structure of NCs with crystal phase D_{4h}. Different outside dielectric constants are considered (blue curves for $\epsilon_2 = 7.3$; green for $\epsilon_2 = 2$; and red for $\epsilon_2 = 1$). (a) Bright states energies, (b) bright-dark splitting δ_{BD}, and (c) bright-bright splitting ΔE, when elongating or reducing the NC size along the Oz direction (or **c** axis).

2. Shape anisotropy, s = 1

Figures 7(a) and 7(b) sum up results for the case $s = 1$ as the r parameter is varied (0.7–1.3 range). The simulation now corresponds to a deformation of the NC along a direction perpendicular to the tetragonal axis of the D_{4h} phase crystal.

In this situation, the degeneracy is, in general, fully lifted and three bright states (associated to linearly polarized transitions) are observed. The calculation highlights a crossing point in the energy plots at $r = 1$, $E_{|Y\rangle} = E_{|X\rangle}$, that is in-

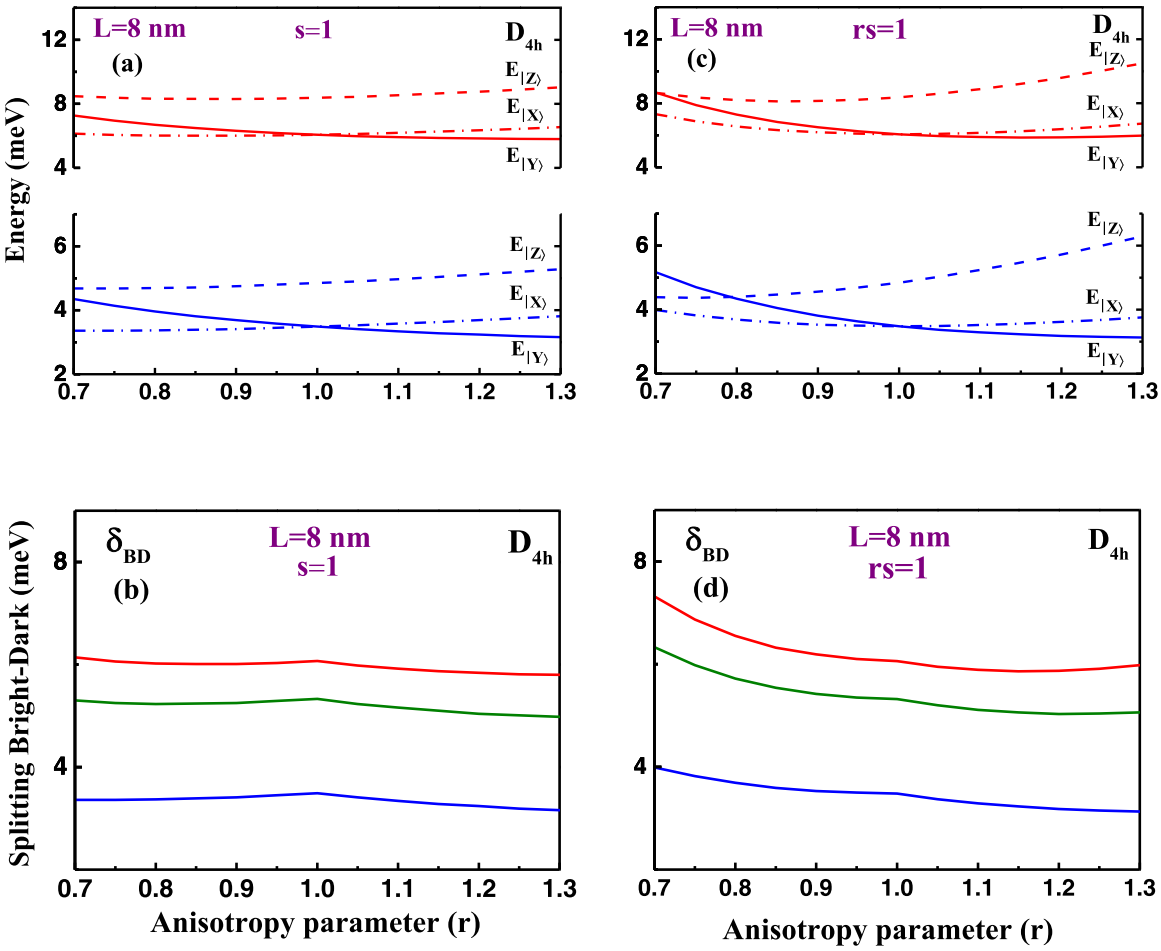

FIG. 7. Exciton fine structure of D_{4h} crystal symmetry NCs. Different contrasts are considered (blue curves for $\epsilon_2 = 7.3$; green for $\epsilon_2 = 2$; red for $\epsilon_2 = 1$). (a) Bright states energies and (b) bright-dark splitting $\delta_{\rm BD}$, when elongating or reducing the NC size along Oy direction. (c) Bright states energies and (d) bright-dark splitting, $\delta_{\rm BD}$, when assuming a shape distortion along two directions in the plane orthogonal to O_x.

dependent of the dielectric contrast. Another crossing point will appear, but is not represented in the Fig. 7(a), between $E_{|Z\rangle}$ and $E_{|Y\rangle}$ at $r < 0.7$. In absence of dielectric contrast the shape anisotropy characterized by the value of r needed to observe the crossing is smaller than in presence of a dielectric contrast. For this two particular values, $r = 1$ and r in the range $r < 0.7$, we obtain two states; a degenerate and a single one.

The $\delta_{\rm BD}$ values are not affected as the deformation axis is changed and again, poor variations ($\simeq 10\%$) are observed in the explored range. The strong amplification of $\delta_{\rm BD}$ resulting from the dielectric confinement is also maintained.

3. Shape effects, rs = 1

The state energetic [depicted in Fig. 7(c)] does not fundamentally differ from the one described in the previous situation: three nondegenerate states are also predicted with $|Y\rangle$ and $|X\rangle$ that are placed at the same energy for $r = 1$ whatever the external dielectric constant may be. We observe a crossing of the $|Y\rangle$ and $|Z\rangle$ states for a smaller deformation (the crossing occurs at $r \simeq 0.7$ when the dielectric contrast is maximal and at $r \simeq 0.8$ in absence of dielectric mismatch). Globally the emission spectrum of a NC and the relative positions of the different states become very sensitive to the NC shape, even for moderate aspect ratio close to 1. Let us finally note that, with regard to the bright state-dark state splitting, an increased sensitivity to the anisotropy is observed for $r < 1$ and close to $r = 0.7$ [Fig. 7(d)].

C. Discussion

Bright-dark splitting in $CsPbBr_3$ NCs with a cubic shape has been recently measured as a function of the edge length thanks to temperature-dependent time-resolved photoluminescence in ensembles [96]. This work in which a simple one-phonon model [97] is used, leads to a clear influence of confinement in determining the bright-dark splitting, increasing from 3.5 to 17 meV, when the NC size varies from 6.5 to 4 nm. It is tempting to try to extrapolate the variation measured as a function of size for the value of 8 nm, considered here for the numerical application, which gives about 2 to 2.5 meV. Even though the crystalline structure of the NCs in the given experimental study is unknown, these

values, although generally lower, are consistent with what is computed here, especially for the tetragonal and orthorhombic symmetries as seen in Figs. 6(b) and 7(b), and this in cases where the dielectric effects are less marked. This final point is relevant since the experiments reported here are conducted on sets of NCs where the dielectric contrast will be lower given the average environment of the NCs.

Recently, Tamarat and coworkers could detect two lines in the photoluminescence spectrum of a single $CsPbBr_3$ NC at low temperature and zero magnetic field (see Supplementary Information of Ref. [43]). One singlet and one doublet could be clearly identified using a magnetic field to lift the doublet degeneracy, but the position of the doublet was shown to change when considering different NCs, being either the highest or the lowest energy line. The authors resorted to a model involving a variation of the shape anisotropy ($r \neq 1$) to explain their results, assuming a O_h symmetry phase of the NCs. This interpretation is fully consistent with the present results (see Fig. 5 and associated comments), however we emphasize that other symmetry conditions could explain their experimental observations, that would also be in better agreement with the results of low temperature structural studies on $CsPbBr_3$ systems.

The tetragonal crystal field can lead to a singlet exciton state polarized linearly along the direction of the crystal axis($|Z\rangle$ state) and to a twofold-degenerate exciton state($|X\rangle$, $|Y\rangle$ doublet). For nearly cubic-shaped NCs or poorly deformed ones along the tetragonal **c** axis the singlet is placed at higher energy [see Fig. 6(a)]. A contribution of tetragonal NCs could thus perfectly explain the different configurations that were experimentally observed in Ref. [43].

More subtle and unlikely scenarios could also be conjectured in the D_{4h} symmetry, as a degeneracy is obtained for point values of the r or rs product parameters. As shown in Fig. 7(c), degenerate states—that will be split under the action of a magnetic field—can indeed be obtained as the higher energy EFS states for a deformation in the plane orthogonal to the **c** axis if $r \simeq 0.7$ and $rs = 1$ for $\epsilon_2 = 1$ or $r \simeq 0.8$ and $rs = 1$ in absence of dielectric mismatch. Then the lower energy line will be associated to the $|X\rangle$ exciton, which is not necessary so when the deformation is considered from the O_h symmetry phase.

As not stated directly in the main text, the extension of the predictions to the orthorhombic structure can be briefly discussed here. When the symmetry is lowered [$\alpha \neq \beta \neq \gamma$ in Eq. (12)] the degeneracy of the EFS levels is fully lifted in perfectly cubic-shaped NCs with states that all correspond to linearly polarized transitions. As the orthorhombic crystal field is small compared to the tetragonal crystal field, a perturbative treatment can be used to deduce the energies of different states. This is done by introducing an additional crystal field term in the tetragonal Hamiltonian (see Supplementary material of Ref. [46]). For $\theta = 40.4°$ (Table I), the $|Z\rangle$ state is then pushed at higher energy whereas $|X\rangle$ and $|Y\rangle$ become the lower energy states (their absolute order remains unknown for it depends of the crystal field perturbation sign that, to the best of our knowledge, is itself still unknown). However, $E_{|X\rangle}$ and $E_{|Y\rangle}$ are poorly changed and remain close since $\alpha \approx \beta$; γ is unchanged in the perturbation development. Let us first consider a deformation along Oz. Then the situation will remain close to the one described for the tetragonal symmetry considering that, once α, β and γ are defined, those are the Λ_i integrals [see Eq. (12)] that pilot the states organization resulting from the NC deformations. It is straightforward to realize that, given the set of values provided in Table I and the assumption that $E_{P_{S,\rho}} \simeq E_{P_{S,z}}$ in the orthorhombic phase, $|Z\rangle$ remains at higher energy and keeps the same dependence with s (decreasing energy as s increases) whereas the energy center of the $|X\rangle$, $|Y\rangle$ pair increases smoothly with increasing s. Thus Fig. 6(a) gives the trend except that the degenerate ($|X\rangle$, $|Y\rangle$) doublet now has to be replaced by a set of two closely spaced states. A double-crossing is thus expected between the $E_{|Z\rangle}$ curve and the lower states ones, occurring for relatively high, close s values. If the deformation is applied along Oy or Ox, moderate changes are again expected in the energetic framework around $r = 1$, for the crystal field effects (± 5 meV shift typically) remain below the energy shifts produced by the deformations; consequently the crossings between the $|X\rangle$ and $|Y\rangle$ levels are no more expected at $r = 1$ [like for the tetragonal symmetry—Figs. 7(a) and 7(c)] but at lower or higher values depending on the sign of the crystal field correction. Calculations become necessary to describe the complete energy behavior if larger deformations are considered, but suppose to know more about the crystal field to be able to reach realistic predictions.

The previous considerations illustrate the difficulty to determine the nature of the involved excitonic states by measuring only the photoluminescence of a single NC. We cannot ignore that a large set of parameters contribute to establish the EFS, among which symmetry, structural (shape) and environmental ones. In this context, it seems that a clear understanding of the photoresponses, including the assignment of the photoluminescence lines, can thus hardly be envisaged without resorting to correlative measurements at the single NC level.

IV. CONCLUSION

We have drawn up a complete picture of the band edge exciton and its fine structure in halide perovskite NCs by taking into consideration the electron-hole exchange interaction (including the short and long range contributions), the crystal symmetry, the effect of dielectric environment, the shape anisotropy and the electronic confinement. This multiparameter framework is a source of complexity but also a richness that provides opportunities for a fine-tuning of the optical properties in this novel class of NCs.

We have shown that (i) the previous treatment of dielectric effects in cuboid perovskite NCs overestimates the long-range EI contribution to the exciton energy, (ii) the bright exciton states splittings are mainly sensitive to the shape anisotropy while the bright dark splitting is impacted by the dielectric mismatch between the NC and the surrounding medium.

This study can serve as a basis for advanced investigations such as those using a magnetic field to explore or control the photoluminescence properties and the EFS by taking into account polaronic effects and varying the dimensionality (0D nanocrystals, nanoplatelets) as in Refs. [39,98,99].

We also emphasize that a correlation between the photoluminescence and electron microscopy measurements—both

performed on the same NC—should be the next step to establish unambiguous connections between the structural parameters (the size but ultimately the crystal phase) and the emitting states structure. Such an approach should definitely allow validating the theoretical approaches and progress in the control of the intrinsic opto-electronic responses.

ACKNOWLEDGMENTS

This work was financially supported by Tunisian Ministry of Higher Education and Scientific Research, the French Ministry of Foreign Affairs through the project PHC Utique (No. 22G1305), and the French National Research Agency (ANR IPER-Nano2, ANR- 18-CE30-0023).

APPENDIX: LONG RANGE EXCHANGE INTERACTION IN PRESENCE OF DIELECTRIC EFFECTS

In presence of a dielectric mismatch, the e-h Coulomb interaction is given by

$$\mathcal{V}_C = -\frac{e^2}{4\pi\epsilon_0\epsilon_1}\sum_{m=-\infty}^{+\infty}\sum_{n=-\infty}^{+\infty}\sum_{p=-\infty}^{+\infty}\frac{\eta^{|m|+|n|+|p|}}{\sqrt{(x_e-x_{hm})^2+(y_e-y_{hn})^2+(z_e-z_{hp})^2}} \tag{A1}$$

with $\eta=(\epsilon_1-\epsilon_2)/(\epsilon_1+\epsilon_2)$ and $x_{hm}=(-1)^m x_y+mL_x$, $y_{hn}=(-1)^n y_h+nL_y$, $z_{hp}=(-1)^p z_h+pL_z$.

The coefficients of the LR matrix [Eq. (9)] can be derived from the general expression of the LR interaction [51,66]

$$\mathcal{H}^{\mathrm{LR}}_{\substack{c'v'\\cv}}\begin{pmatrix}\mathbf{r}'_e & \mathbf{r}'_h\\ \mathbf{r}_e & \mathbf{r}_h\end{pmatrix}=\sum_{i,j}\mathfrak{Q}^{ij}_{\substack{c'\mathcal{I}v\\ \mathcal{I}v'c}}\frac{\partial^2}{\partial r^i_e\partial r^j_h}\mathcal{W}(\mathbf{r}_e,\mathbf{r}'_h)\,\delta(\mathbf{r}_e-\mathbf{r}_h)\delta(\mathbf{r}'_e-\mathbf{r}'_h), \tag{A2}$$

where $\mathcal{W}$ is derived from $(-\mathcal{V}_C)$ by replacing ϵ_1 by ϵ_X (dielectric constant at the exciton resonance) in the denominator; c, c′ (v,v′) label the Bloch states in the conduction band (the hole in the valence band), and $(\mathbf{r}_e,\mathbf{r}'_e)$ and $(\mathbf{r}_h,\mathbf{r}'_h)$ denotes the coordinates of the electrons and holes, respectively. $\mathcal{I}$ is the time-reversal operator; it leaves **r** unchanged but changes the kinetic momentum **p** and the angular momentum in their opposite. The $\mathfrak{Q}$ matrix encloses the products of momentum operators [87,100], their matrix elements are given by

$$\mathfrak{Q}^{ij}_{\substack{c'\mathcal{I}v\\ \mathcal{I}v'c}}=\frac{\hbar^2}{m_0^2}\frac{\langle c'|p_i|\mathcal{I}v'\rangle\langle\mathcal{I}v|p_j|c\rangle}{\left(E^0_c-E^0_v\right)\left(E^0_{c'}-E^0_{v'}\right)}, \tag{A3}$$

where m_0 is the free electron mass, p_i (p_j) is the i (j) component of the **p** momentum; E^0_ν $(\nu=c,c',v,v')$ is the ν^{th} band energy.

To derive the expression of the LR Hamiltonian, it is then necessary to calculate $\partial^2\mathcal{W}/\partial r^i_e\partial r^j_h$. First, the interaction $\mathcal{W}$ can be rewritten, using the Fourier transform

$$\mathcal{W}(\mathbf{r}_e,\mathbf{r}'_h)=\frac{1}{(2\pi)^3}\frac{e^2}{\epsilon_0\epsilon_X}\int\frac{d\mathbf{q}}{q^2}\sum_{m=-\infty}^{+\infty}\sum_{n=-\infty}^{+\infty}\sum_{p=-\infty}^{+\infty}\eta^{|m|+|n|+|p|}\exp iq_x(x_e-x'_{hm})\exp iq_y(y_e-y'_{hn})\exp iq_z(z_e-z'_{hp}). \tag{A4}$$

One deduces

$$\frac{\partial^2\mathcal{W}}{\partial r^i_e\partial r^j_h}(\mathbf{r}_e,\mathbf{r}'_h)=-\frac{1}{(2\pi)^3}\frac{e^2}{\epsilon_0\epsilon_X}\int d\mathbf{q}\frac{q_iq_j}{q^2}\sum_{m=-\infty}^{+\infty}\sum_{n=-\infty}^{+\infty}\sum_{p=-\infty}^{+\infty}(-1)^{\ell_j}\eta^{|m|+|n|+|p|}\exp iq_x(x_e-x'_{hm})\exp iq_y(y_e-y'_{hn})\exp iq_z(z_e-z'_{hp}) \tag{A5}$$

with $\ell_j=m$, n, or p, for $j=x$, y, or z, respectively.

Knowing the e-h envelope wave-function, the $\mathcal{H}^{\mathrm{LR}}$ matrix elements are then

$$\begin{aligned}&-\frac{1}{(2\pi)^3}\frac{e^2}{\epsilon_0\epsilon_X}\int\frac{d\mathbf{q}}{q^2}\sum_{i,j}\mathfrak{Q}^{ij}_{\substack{c'\mathcal{I}v\\ \mathcal{I}v'c}}q_iq_j\sum_{m=-\infty}^{+\infty}\sum_{n=-\infty}^{+\infty}\sum_{p=-\infty}^{+\infty}(-1)^{\ell_j}\eta^{|m|+|n|+|p|}\exp(-iq_xL_x)\exp(-iq_yL_y)\exp(-iq_zL_z)\\ &\times\int d\mathbf{r}\Psi(\mathbf{r},\mathbf{r})\exp(\mathbf{iq}.\mathbf{r})\int d\mathbf{r}\Psi(\mathbf{r},\mathbf{r})\exp(\mathbf{iq}.\xi_{m,n,p})\end{aligned} \tag{A6}$$

with

$$\xi_{m,n,p}=((-1)^m x,(-1)^n y,(-1)^p z). \tag{A7}$$

Due to the parity of the function $\Psi(\mathbf{r},\mathbf{r})$, both **r** integrals in (A6) are equal and can be isolated from the three discrete summations. Summing separately on the integers m, n, and p, one obtains

$$-\frac{1}{(2\pi)^3}\frac{e^2}{\epsilon_0\epsilon_X}\int\frac{d\mathbf{q}}{q^2}\sum_{i,j}\mathfrak{Q}^{ij}_{\substack{c'\mathcal{I}v\\ \mathcal{I}v'c}}q_iq_j\prod_{\alpha=x,y,z}\mathfrak{D}_\alpha(q_\alpha,L_\alpha)\left|\int d\mathbf{r}\Psi(\mathbf{r},\mathbf{r})\exp(\mathbf{iq}.\mathbf{r})\right|^2 \tag{A8}$$

with

$$\mathfrak{D}_\alpha(q_\alpha, L_\alpha) = \begin{cases} \mathfrak{D}_+(q_\alpha, L_\alpha) = \frac{(1-\eta^2)}{1+\eta^2+2\eta\cos(q_\alpha L_\alpha)} & \text{for } \alpha = j \\ \mathfrak{D}_-(q_\alpha, L_\alpha) = \frac{(1-\eta^2)}{1+\eta^2-2\eta\cos(q_\alpha L_\alpha)} & \text{for } \alpha \neq j \end{cases}. \tag{A9}$$

The explicit form of the matrix representation of $\mathfrak{Q}_{\substack{c'\mathcal{I}v \\ \mathcal{I}v'c}}(\mathbf{q}) = \sum_{i,j}\mathfrak{Q}^{ij}_{\substack{c'\mathcal{I}v \\ \mathcal{I}v'c}} q_i q_j$ in the basis $\{|+1\rangle, |-1\rangle, |0_B\rangle, |0_D\rangle\}$ is

$$\frac{1}{E_g^2}\begin{bmatrix} \begin{pmatrix}\alpha^2 P_{S,x}^2 q_x^2 \\ +\beta^2 P_{S,y}^2 q_y^2\end{pmatrix} & -\begin{pmatrix}\alpha P_{S,x} q_x \\ -i\beta P_{S,y} q_y\end{pmatrix}^2 & \sqrt{2}\gamma P_{S,z} q_z \begin{pmatrix}\alpha P_{S,x} q_x \\ -i\beta P_{S,y} q_y\end{pmatrix} & 0 \\ \text{c.c.} & \begin{pmatrix}\alpha^2 P_{S,x}^2 q_x^2 \\ +\beta^2 P_{S,y}^2 q_y^2\end{pmatrix} & -\sqrt{2}\gamma P_{S,z} q_z \begin{pmatrix}\alpha P_{S,x} q_x \\ +i\beta P_{S,y} q_y\end{pmatrix} & 0 \\ \text{c.c.} & c.c. & 2\gamma^2 P_{S,z}^2 q_z^2 & 0 \\ 0 & 0 & 0 & 0 \end{bmatrix}, \tag{A10}$$

where c.c. denotes the complex conjugate. $(P_{S,x}, P_{S,y}, P_{S,z})$ are the nonzero matrix elements of the momentum operator $\mathbf{p}$ according to the D_{2h} point group symmetry [53]. In O_h symmetry, all these matrix elements are equals, while in D_{4h} symmetry $P_{S,x} = P_{S,y} = P_{S,\rho}$.

This lead to the following LR matrix

$$\mathcal{H}^{\text{LR}} = \begin{bmatrix} \Sigma_d & \Sigma_{od} & 0 & 0 \\ \Sigma_{od} & \Sigma_d & 0 & 0 \\ 0 & 0 & \Sigma_z & 0 \\ 0 & 0 & 0 & 0 \end{bmatrix} \tag{A11}$$

and the matrix elements

$$\begin{aligned} \Sigma_d &= \left[\alpha^2 E_{P_{S,x}} I_x + \beta^2 E_{P_{S,y}} I_y\right]\Lambda\pi^9\left(\frac{\pi a_X^3}{L_x^3}\right)\left(\frac{3|\mathcal{N}(a)|^2}{rs}\right) \\ \Sigma_{od} &= \left[-\alpha^2 E_{P_{S,x}} I_x + \beta^2 E_{P_{S,y}} I_y\right]\Lambda\pi^9\left(\frac{\pi a_X^3}{L_x^3}\right)\left(\frac{3|\mathcal{N}(a)|^2}{rs}\right) \\ \Sigma_z &= 2\gamma^2 E_{P_{S,z}} I_z \Lambda\pi^9\left(\frac{\pi a_X^3}{L_x^3}\right)\left(\frac{3|\mathcal{N}(a)|^2}{rs}\right) \end{aligned} \tag{A12}$$

with

$$\Lambda = \frac{1}{3E_g^2}\frac{\hbar^2}{2m_0}\frac{e^2}{\epsilon_0\epsilon_X}\frac{1}{\pi a_X^3}. \tag{A13}$$

The exchange integrals I_j $(j = x, y, z)$ are expressed as

$$\begin{aligned} I_x &= \int d\mathbf{u}\frac{r^2 s^2 u_x^2}{r^2 s^2 u_x^2 + s^2 u_y^2 + r^2 u_z^2}\frac{\sin^2 u_x}{u_x^2\left(u_x^2-\pi^2\right)^2}\frac{\sin^2 u_y}{u_y^2\left(u_y^2-\pi^2\right)^2}\frac{\sin^2 u_z}{u_z^2\left(u_z^2-\pi^2\right)^2} d_+(u_x) d_-(u_y) d_-(u_z) \\ I_y &= \int d\mathbf{u}\frac{s^2 u_y^2}{r^2 s^2 u_x^2 + s^2 u_y^2 + r^2 u_z^2}\frac{\sin^2 u_x}{u_x^2\left(u_x^2-\pi^2\right)^2}\frac{\sin^2 u_y}{u_y^2\left(u_y^2-\pi^2\right)^2}\frac{\sin^2 u_z}{u_z^2\left(u_z^2-\pi^2\right)^2} d_-(u_x) d_+(u_y) d_-(u_z) \\ I_z &= \int d\mathbf{u}\frac{r^2 u_z^2}{r^2 s^2 u_x^2 + s^2 u_y^2 + r^2 u_z^2}\frac{\sin^2 u_x}{u_x^2\left(u_x^2-\pi^2\right)^2}\frac{\sin^2 u_y}{u_y^2\left(u_y^2-\pi^2\right)^2}\frac{\sin^2 u_z}{u_z^2\left(u_z^2-\pi^2\right)^2} d_-(u_x) d_-(u_y) d_+(u_z) \end{aligned} \tag{A14}$$

in which $d_\pm(u) = (1-\eta^2)/(1+\eta^2 \pm 2\eta\cos(2u))$.

[1] A. Kojima, K. Teshima, Y. Shirai, and T. Miyasaka, J. Am. Chem. Soc. **131**, 6050 (2009).

[2] H.-S. Kim, C.-R. Lee, J.-H. Im, K.-B. Lee, T. Moehl, A. Marchioro, S.-J. Moon, R. Humphry-Baker, J.-H. Yum, J. E. Moser, M. Grätzel, and N.-G. Park, Sci. Rep. **2**, 591 (2012).

[3] M. M. Lee, J. Teuscher, T. Miyasaka, T. N. Murakami, and H. J. Snaith, Science **338**, 643 (2012).

[4] Z.-K. Tan, R. S. Moghaddam, M. L. Lai, P. Docampo, R. Higler, F. Deschler, M. Price, A. Sadhanala, L. M. Pazos, D. Credgington, F. Hanusch, T. Bein, H. J. Snaith, and R. H. Friend, Nat. Nanotechnol. **9**, 687 (2014).

[5] S. D. Stranks and H. J. Snaith, Nat. Nanotechnol. **10**, 391 (2015).

[6] K. Lin, J. Xing, L. N. Quan, F. P. G. de Arquer, X. W. Gong, J. X. Lu, L. Q. Xie, W. J. Zhao, D. Zhang, C. Z. Yan, W. Q. Li, X. Y. Liu, Y. Lu, J. Kirman, E. H. Sargent, Q. H. Xiong, and Z. H. Wei, Nature (London) **562**, 245 (2018).

[7] H. Zhu, Y. Fu, F. Meng, X. Wu, Z. Gong, Q. Ding, M. V. Gustafsson, M. T. Trinh, S. Jin, and X.-Y. Zhu, Nat. Mater. **14**, 636 (2015).

[8] G. Xing, N. Mathews, S. S. Lim, N. Yantara, X. Liu, D. Sabba, M. Gratzel, S. Mhaisalkar, and T. C. Sum, Nat. Mater. **13**, 476 (2014).

[9] L. Dou, Y. M. Yang, J. You, Z. Hong, W. Chang, G. Li, and Y. Yang, Nat. Commun. **5**, 5404 (2014).

[10] Y. Fang, Q. Dong, Y. Shao, Y. Yuan, and J. Huang, Nat. Photonics **9**, 679 (2015).

[11] M. Kepenekian, R. Robles, C. Katan, D. Sapori, L. Pedesseau, and J. Even, ACS Nano **9**, 11557 (2015).

[12] M. Kepenekian and J. Even, J. Phys. Chem. Lett. **8**, 3362 (2017).

[13] G. Garcia-Arellano, G. Trippé-Allard, L. Legrand, T. Barisien, D. Garrot, E. Deleporte, F. Bernardot, C. Testelin, and M. Chamarro, J. Phys. Chem. Lett. **12**, 8272 (2021).

[14] J.-H. Im, C.-R. Lee, J.-W. Lee, S.-W. Park, and N.-G. Park, Nanoscale **3**, 4088 (2011).

[15] L. C. Schmidt, A. Pertegas, S. Gonzalez-Carrero, O. Malinkiewicz, S. Agouran, C. Minguez Espallargas, H. J. Bolink, R. E. Galian, and J. Pérez-Prieto, J. Am. Chem. Soc. **136**, 850 (2014).

[16] Q. A. Akkerman, G. Rainò, M. V. Kovalenko, and L. Manna, Nat. Mater. **17**, 394 (2018).

[17] Q. A. Akkerman, S. Genaro Motti, A. R. S. Kandada, E. Mosconi, V. D'Innocenzo, G. Bertoni, S. Marras, B. A. Kamino, L. Miranda, F. De Angelis, A. Petrozza, M. Prato, and L. Manna, J. Am. Chem. Soc. **138**, 1010 (2016).

[18] D. Zhang, S. W. Eaton, Y. Yu, L. Dou, and P. Yang, J. Am. Chem. Soc. **137**, 9230 (2015).

[19] F. Brivio, K. T. Butler, A. Walsh, and M. van Schilfgaarde, Phys. Rev. B **89**, 155204 (2014).

[20] W.-J. Yin, J.-H. Yang, J. Kang, Y. Yan, and S.-W. Wei, J. Mater. Chem. A **3**, 8926 (2015).

[21] L.-Y. Huang and W. R. L. Lambrecht, Phys. Rev. B **93**, 195211 (2016).

[22] M. Shirayama, H. Kadowaki, T. Miyadera, T. Sugita, M. Tamakoshi, M. Kato, T. Fujiseki, D. Murata, S. Hara, T. N. Murakami, S. Fujimoto, M. Chikamatsu, and H. Fujiwara, Phys. Rev. Appl. **5**, 014012 (2016).

[23] J. Even, L. Pedesseau, J.-M. Jancu, and C. Katan, J. Phys. Chem. Lett. **4**, 2999 (2013).

[24] R. Ben Aich, S. Ben Radhia, K. Boujdaria, M. Chamarro, and C. Testelin, J. Phys. Chem. Lett. **11**, 808 (2020).

[25] S. Meloni, G. Palermo, N. Ashari-Astani, M. Grätzelb, and U. Rothlisberger, J. Mater. Chem. A **4**, 15997 (2016).

[26] M. Baranowski and P. Plochocka, Adv. Energy Mater. **10**, 1903659 (2020).

[27] M. Baranowski, P. Plochocka, R. Su, L. Legrand, T. Barisien, F. Bernardot, Q. Xiong, C. Testelin, and M. Chamarro, Photonics Res. **8**, A50 (2020).

[28] C. K. Møller, Nature (London) **182**, 1436 (1958).

[29] Y. Fujii, S. Hoshino, Y. Yamada, and G. Shirane, Phys. Rev. B **9**, 4549 (1974).

[30] S. Hirotsu, J. Harada, M. Iizumi, and K. Gesi, J. Phys. Soc. Jpn. **37**, 1393 (1974).

[31] C. C. Stoumpos, C. D. Malliakas, J. A. Peters, Z. Liu, M. Sebastian, J. Im, T. C. Chasapis, A. C. Wibowo, D. Y. Chung, A. J. Freeman, B. W. Wessels, and M. G. Kanatzidis, Crystal Growth and Design **13**, 2722 (2013).

[32] J. Even, L. Pedesseau, C. Katan, M. Kepenekian, J.-S. Laurent, D. Sapori, and E. Deleporte, J. Phys. Chem. C **119**, 10161 (2015).

[33] J. Even, J. Phys. Chem. Lett. **6**, 2238 (2015).

[34] J. Qian, B. Xu, and W. Tian, Org. Electron. **37**, 61 (2016).

[35] M. Baranowski, K. Galkowski, A. Surrente, J. Urban, L. Klopotowski, S. Maćkowski, D. K. Maude, R. Ben Aich, K. Boujdaria, M. Chamarro, C. Testelin, P. K. Nayak, M. Dollmann, H. J. Snaith, R. J. Nicholas, and P. Plochocka, Nano Lett. **19**, 7054 (2019).

[36] L. Protesescu, S. Yakunin, M. I. Bodnarchuk, F. Krieg, R. Caputo, C. H. Hendon, R. X. Yang, A. Walsh, and M. V. Kovalenko, Nano Lett. **15**, 3692 (2015).

[37] M. Fu, P. Tamarat, J.-P. Trebbia, M. I. Bodnarchuk, M. V. Kovalenko, J. Even, and B. Lounis, Nat. Commun. **9**, 3318 (2018).

[38] O. Pfingsten, J. Klein, L. Protesescu, M. I. Bodnarchuk, M. V. Kovalenko, and G. Bacher, Nano Lett. **18**, 4440 (2018).

[39] P. Tamarat, M. I. Bodnarchuk, J.-B. Trebbia, R. Erni, M. V. Kovalenko, J. Even, and B. Lounis, Nat. Mater. **18**, 717 (2019).

[40] L. Liu, F. Pevere, F. Zhang, H. Zhong, and I. Sychugov, Phys. Rev. B **100**, 195430 (2019).

[41] L. Liu, R. Zhao, C. Xiao, F. Zhang, F. Pevere, K. Shi, H. Huang, H. Zhong, and I. Sychugov, J. Phys. Chem. Lett. **10**, 5451 (2019).

[42] C. Yin, L. Chen, N. Song, Y. Lv, F. Hu, C. Sun, W. W. Yu, C. Zhang, X. Wang, Y. Zhang, and M. Xiao, Phys. Rev. Lett. **119**, 026401 (2017).

[43] P. Tamarat, L. Hou, J.-P. Trebia, A. Swarnkar, L. Biadala, Y. Louyer, M. I. Bodnarchuk, M. V. Kovalenko, J. Even, and B. Lounis, Nat. Commun. **11**, 6001 (2020).

[44] M. Isarov, L. Z. Tan, M. I. Bodnarchuk, M. V. Kovalenko, A. M. Rappe, and E. Lifshitz, Nano Lett. **17**, 5020 (2017).

[45] M. Fu, P. Tamarat, H. Huang, J. Even, A. L. Rogach, and B. Lounis, Nano Lett. **17**, 2895 (2017).

[46] J. Ramade, L. M. Andriambariarijaona, V. Steinmetz, N. Goubet, L. Legrand, T. Barisien, F. Bernardot, C. Testelin, E. Lhuillier, A. Bramati, and M. Chamarro, Nanoscale **10**, 6393 (2018).

[47] J. Ramade, L. M. Andriambariarijaona, V. Steinmetz, N. Goubet, L. Legrand, T. Barisien, F. Bernardot, C. Testelin, E. Lhuillier, A. Bramati, and M. Chamarro, Appl. Phys. Lett. **112**, 072104 (2018).

[48] G. Rainò, G. Nedelcu, L. Protesescu, M. I. Bodnarchuk, M. V. Kovalenko, R. F. Mahrt, and T. Stöferle, ACS Nano **10**, 2485 (2016).

[49] M. A. Becker, R. Vaxenburg, G. Nedelcu, P. C. Sercel, A. Shabaev, M. J. Mehl, J. G. Michopoulos, S. G. Lambrakos, N. Bernstein, J. L. Lyons, T. Stöferle, R. F. Mahrt, M. V.

Kovalenko, D. J. Norris, G. Rainò, and A. L. Efros, Nature (London) **553**, 189 (2018).
[50] T. Takagahara, Phys. Rev. B **47**, 4569 (1993).
[51] H. Tong and M. W. Wu, Phys. Rev. B **83**, 235323 (2011).
[52] M. Chamarro, C. Gourdon, P. Lavallard, O. Lublinskaya, and A. I. Ekimov, Phys. Rev. B **53**, 1336 (1996).
[53] R. Ben Aich, I. Saïdi, S. Ben Radhia, K. Boujdaria, T. Barisien, L. Legrand, F. Bernardot, M. Chamarro, and C. Testelin, Phys. Rev. Appl. **11**, 034042 (2019).
[54] K. Xu, J. F. Vlien, and A. Meijerink, J. Phys. Chem. C **123**, 979 (2019).
[55] P. C. Sercel, J. L. Lyons, D. Wickramaratne, R. Vaxenburg, N. Bernstein, and A. L. Efros, Nano Lett. **19**, 4068 (2019).
[56] S. T. Ha, X. Liu, Q. Zhang, D. Giovanni, T. C. Sum, and Q. Xion, Adv. Opt. Mater. **2**, 838 (2014).
[57] V. A. Hintermayr, A. F. Richter, F. Ehrat, M. Döblinger, W. Vanderlinden, J. A. Sichert, Y. Tong, L. Polavarapu, J. Feldmann, and A. S. Urban, Adv. Mater. **28**, 9478 (2016).
[58] M. B. Teunis, A. Jana, P. Dutta, M. A. Johnson, M. Mandal, B. B. Muhoberac, and R. Sardar, Chem. Mater. **28**, 5043 (2016).
[59] Y. Tong, M. Fu, E. Bladt, H. Huang, A. F. Richter, K. Wang, P. Müller-Buschbaum, S. Bals, P. Tamarat, B. Lounis, J. Feldmann, and L. Polavarapu, Angew. Chem. **130**, 16326 (2018).
[60] F. Bertolotti, G. Nedelcu, A. Vivani, A. Cervellino, N. Masciocchi, A. Guagliardi, and M. V. Kovalenko, ACS Nano **13**, 14294 (2019).
[61] C. Huo, C. F. Fong, M.-R. Amara, Y. Huang, B. Chen, H. Zhang, L. Guo, H. Li, W. Huang, C. Diederichs, and Q. Xiong, Nano Lett. **20**, 3673 (2020).
[62] J. Hu, L. Li, W. Yang, L. Manna, L. Wang, and A. P. Alivisatos, Science **292**, 2060 (2001).
[63] R. Scott, J. Heckmann, A. V. Prudnikau, A. Antanovich, A. Mikhailov, N. Owschimikow, M. Artemyev, J. I. Climente, U. Woggon, N. B. Grosse, and A. W. Achtstein, Nat. Nanotechnol. **12**, 1155 (2017).
[64] M. O. Nestoklon, S. V. Goupalov, R. I. Dzhioev, O. S. Ken, V. L. Korenev Yu., G. Kusrayev, V. F. Sapega, C. de Weerd, L. Gomez, T. Gregorkiewicz, J. Lin, K. Suenaga, Y. Fujiwara, L. B. Matyushkin, and I. N. Yassievich, Phys. Rev. B **97**, 235304 (2018).
[65] P. C. Sercel, J. L. Lyons, N. Bernstein, and A. L. Efros, J. Chem. Phys. **151**, 234106 (2019).
[66] S. V. Gupalov and E. L. Ivchenko, Phys. Solid State **42**, 2030 (2000).
[67] M. Liao, B. Shan, and M. Li, J. Phys. Chem. Lett. **10**, 1217 (2019).
[68] X. Blase, I. Duchemin, D. Jacquemin, and P.-F. Loos, J. Phys. Chem. Lett. **11**, 7371 (2020).
[69] X. Leng, F. Jin, M. Wei, and Y. Ma, WIREs Comput. Mol. Sci. **6**, 532 (2016).
[70] H. Bui, A. Karpulevich, and G. Bester, Phys. Rev. B **101**, 115414 (2020).
[71] P. Han, J. Min, Z. Zeng, C. S. Garoufalis, S. Baskoutas, Y. Jia, and Z. Du, Phys. Rev. B **104**, 045404 (2021).
[72] X. Ma, J. Min, Z. Zeng, C. S. Garoufalis, S. Baskoutas, Y. Jia, and Z. Du, Phys. Rev. B **100**, 245404 (2019).
[73] I. D. Avdeev, M. O. Nestoklon, and S. V. Goupalov, Nano Lett. **20**, 8897 (2020).
[74] A. Franceschetti and A. Zunger, Phys. Rev. Lett. **78**, 915 (1997).
[75] X. Zhu, G. A. Chass, L.-C. Kwek, A. L. Rogach, and H. Su, J. Phys. Chem. C **119**, 29171 (2015).
[76] V. Steinmetz, J. Ramade, L. Legrand, T. Barisien, F. Bernardot, E. Lhuillier, M. Bernard, M. Vabre, I. Saidi, A. Ghribi, K. Boujdaria, C. Testelin, and M. Chamarro, Nanoscale **12**, 18978 (2020).
[77] I. Saïdi, S. Ben Radhia, and K. Boujdaria, J. Appl. Phys. **107**, 043701 (2010).
[78] R. Neffati, I. Saïdi, and K. Boujdaria, J. Appl. Phys. **112**, 053716 (2012).
[79] A. Ghribi, R. Ben Aich, K. Boujdaria, T. Barisien, L. Legrand, M. Chamarro, and C. Testelin, Nanomaterials **11**, 3054 (2021).
[80] G. Mannino, I. Deretzis, E. Smecca, A. La Magna, A. Alberti, D. Ceratti, and D. Cahen, J. Phys. Chem. Lett. **11**, 2490 (2020).
[81] Z. Yang, A. Surrente, K. Galkowski, A. Miyata, O. Portugall, R. J. Sutton, A. A. Haghighirad, H. J. Snaith, D. K. Maude, P. Plochocka, and R. J. Nicholas, ACS Energy Lett. **2**, 1621 (2017).
[82] X. Chen, Y. Wang, J. Song, X. Li, J. Xu, H. Zeng, and H. Sun, J. Phys. Chem. C **123**, 10564 (2019).
[83] M. Kumagai and T. Takagahara, Phys. Rev. B **40**, 12359 (1989).
[84] F. Rajadell, J. I. Climente, and J. Planelles, Phys. Rev. B **96**, 035307 (2017).
[85] B. Traore, J. Even, L. Pedesseau, M. Kepenekian, and C. Katan, Phys. Rev. Mater. **6**, 014604 (2022).
[86] X. Liu, H. Zhao, L. Wei, X. Ren, X. Zhang, F. Li, P. Zeng, and M. Liu, Nanophotonics **10**, 1967 (2021).
[87] G. E. Pikus and G. L. Bir, Zh. Eksp. Teor. Fiz. **60**, 195 (1971) [Sov. Phys. JETP **33**, 108 (1971)].
[88] G. L. Bir and G. E. Pikus, *Symmetry and Strain Induced Effects in Semiconductors* (Wiley, New York, 1975).
[89] M. M. Denisov and V. P. Makarov, Phys. Stat. Sol. (b) **56**, 9 (1973).
[90] Y. Chen, B. Gil, P. Lefebvre, and H. Mathieu, Phys. Rev. B **37**, 6429 (1988).
[91] S. V. Gupalov, E. L. Ivchenko, and A. V. Kavokin, J. Exp. Theor. Phys. **86**, 388 (1998).
[92] A. L. Efros, M. Rosen, M. Kuno, M. Nirmal, D. J. Norris, and M. Bawendi, Phys. Rev. B **54**, 4843 (1996).
[93] R. Romestain and G. Fishman, Phys. Rev. B **49**, 1774 (1994).
[94] H. Mekni, A. Pankratov, S. Ben Radhia, K. Boujdaria, M. Chamarro, and C. Testelin, Phys. Rev. B **103**, 075302 (2021).
[95] U. Rössler and H.-R. Trebin, Phys. Rev. B **23**, 1961 (1981).
[96] D. Rossi, T. Qiao, X. Liu, M. Khurana, A. V. Akimov, J. Cheon, and D. H. Son, J. Chem. Phys. **153**, 184703 (2020).
[97] O. Labeau, P. Tamarat, and B. Lounis, Phys. Rev. Lett. **90**, 257404 (2003).
[98] R. Butler, R. Burns, D. Babaian, M. J. Anderson, C. A. Ullrich, M. V. Morell, Y. Xing, J. Lee, and S. Guha, J. Appl. Phys. **131**, 125105 (2022).
[99] S. Wang, M. Dyksik, C. Lampe, M. Gramlich, D. K. Maude, M. Baranowski, A. S. Urban, P. Plochocka, and A. Surrente, Nano Lett. **22**, 7011 (2022).
[100] S. V. Goupalov and E . L. Ivchenko, J. Cryst. Growth **184–185**, 393 (1998).